Bulletin of the Seismological Society of America, Vol. 95, No. 2, pp. 446–470, April 2005, doi: 10.1785/0120020202

Ⓔ

Subsurface Structure and Kinematics of the Calaveras–Hayward Fault Stepover from Three-Dimensional V_p and Seismicity, San Francisco Bay Region, California

by David M. Manaker, Andrew J. Michael, and Roland Bürgmann

Abstract The Calaveras and Hayward faults are major components of the San Andreas fault system in the San Francisco Bay region. Dextral slip is presumed to transfer from the Calaveras fault to the Hayward fault in the Mission Hills region, an area of uplift in the contractional stepover between the two faults. Here the estimated deep slip rates drop from 15 to 6 mm/yr on the Calaveras fault, and slip begins on the Hayward fault at an estimated 9 mm/yr. A lineament of microseismicity near the Mission fault links the seismicity on the Calaveras and Hayward faults and is presumed to be related directly to this slip transfer. However, geologic and seismologic evidence suggest that the Mission fault may not be the source of the seismicity and that the Mission fault is not playing a major role in the slip transfer.

We perform a joint inversion for hypocenters and the 3D *P*-wave velocity structure of the stepover region using 477 earthquakes. We find strong velocity contrasts across the Calaveras and Hayward faults, corroborated by geologic, gravity, and aeromagnetic data. Detailed examination of two seismic lineaments in conjunction with the velocity model and independent geologic and geophysical evidence suggests that they represent the southern extension of a northeasterly dipping Hayward fault that splays off the Calaveras fault, directly accounting for the deep slip transfer. The Mission fault appears to be accommodating deformation within the block between the Hayward and Calaveras faults. Thus, the Calaveras and Hayward faults need to be considered as a single system for developing rupture scenarios for seismic hazard assessments.

Online material: 3D interactive visualizations of the Mission and Alum Rock hypocenters.

Introduction

Fault systems at plate boundaries typically accommodate a wide range of deformational styles. In central California, the primary style of deformation is due to transform faulting. These faults exhibit bends, jogs, stepovers, and splays, resulting in regions of complex deformation. In the San Francisco Bay region, the interaction between the Calaveras and Hayward faults produces such a region. This study examines how the Calaveras and Hayward faults interact, how slip is transferred between them, and its implications for seismic hazard assessment.

The Calaveras and Hayward faults overlap for a length of ~60 km, bounding the East Bay Hills in a restraining stepover region (Aydin and Page, 1984) (Figs. 1 and 2). The southeast 20 km of the overlap between these two strike-slip faults bound the Mission Hills that border the eastern San Francisco Bay alluvial plain (Fig. 1). Here the surface traces of the two faults are 3–5 km apart and the interaction between the faults produces contractional structures (Aydin and Page, 1984; Kelson *et al.*, 1993). The contraction in the Mission Hills due to local fault interaction is accommodated by folding and reverse faulting (Jones *et al.*, 1994).

Although the most significant seismic threat in the San Francisco Bay region is due to earthquakes occurring on right-lateral, strike-slip faults, an additional hazard exists because of reverse faulting in the California Coast Ranges. Several recent damaging earthquakes in California involve a significant component of dip slip. Examples include the 1983 (M_W 6.7) Coalinga (Sipkin and Needham, 1990), 1987 (M_L 5.9) Whittier Narrows (Hauksson *et al.*, 1988), 1989 (M_W 6.9) Loma Prieta (Ellsworth, 1990), 1994 (M_W 6.7) Northridge (Hauksson *et al.*, 1995), and 2003 (M_W 6.5) San Simeon earthquakes (Hardebeck *et al.*, 2004). These events

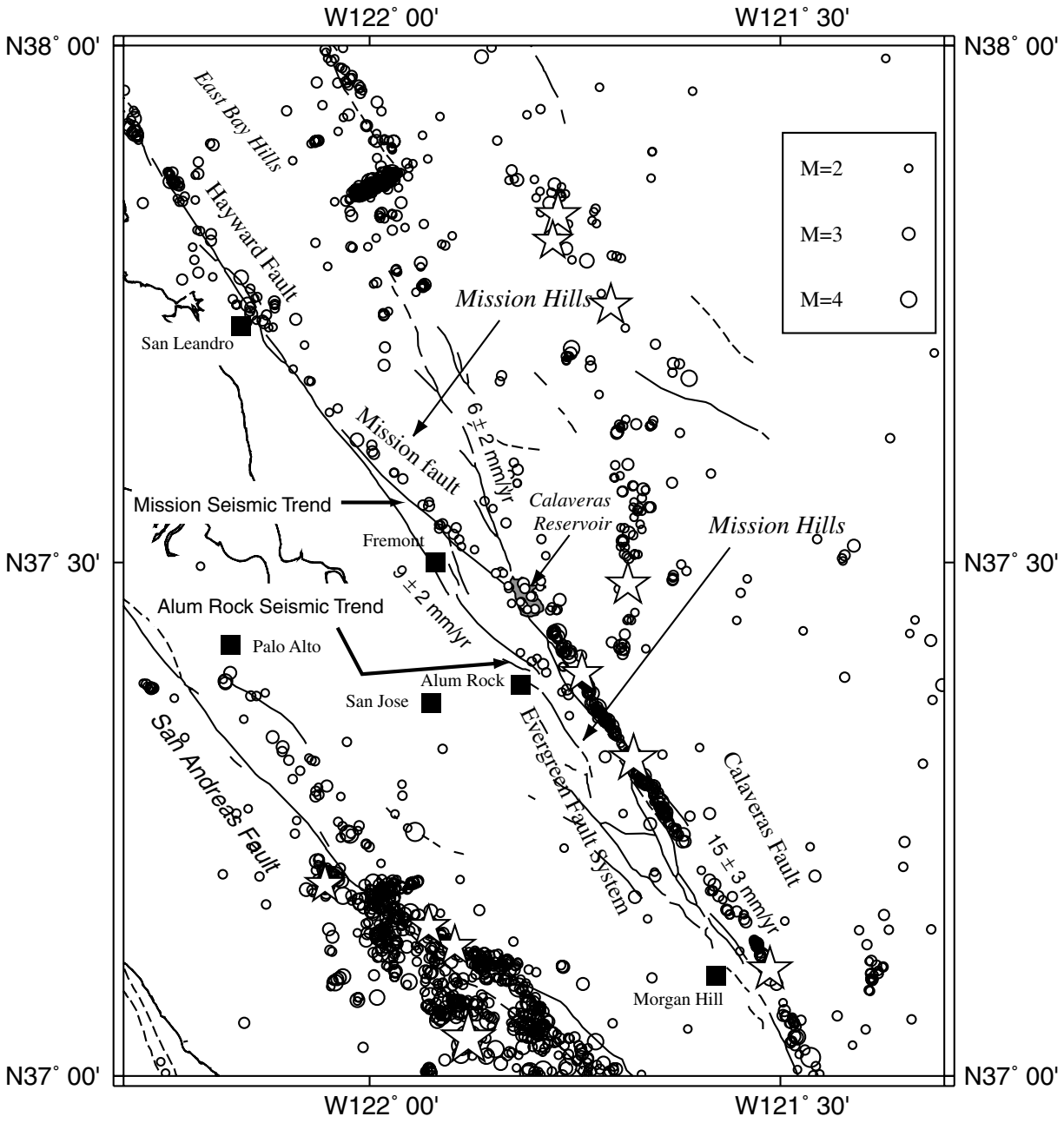

Figure 1. Calaveras-Hayward fault stepover region and its relation to principal urban areas of the southern San Francisco Bay region. Heavy lines represent mapped faults of the region. Fault slip rate shown next to faults from Working Group on California Earthquake Probabilities (1999). Seismicity shown is for events $M_D \geq 2$ from 1984 to 1998. Significant earthquakes ($M_W > 5$) since 1979 are shown by stars. Locations shown are from the NCSN catalog obtained from Northern California Earthquake Data Center operated by the Berkeley Seismological Station (http://quake.geo.berkeley.edu/ncedc/catalog-search.html).

illustrate the seismic threat from reverse faulting in contractional regions along transform plate boundaries.

Recognizing the potential seismic hazard due to reverse faulting in the San Francisco Bay region, Andrews *et al.* (1993) evaluated such a hazard for the Calaveras-Hayward fault stepover region. Through an analysis of fault geometries and slip rates, they calculated a hypothetical dip-slip event in the region from the accumulated dip-slip deficit. Based on a seismogenic depth of 10 km, the horizontal shortening accumulated over 150 years would produce a M_W 6.3 event if the entire slip deficit was released in a single event. Additionally, they hypothesize that a dip-slip event may trig-

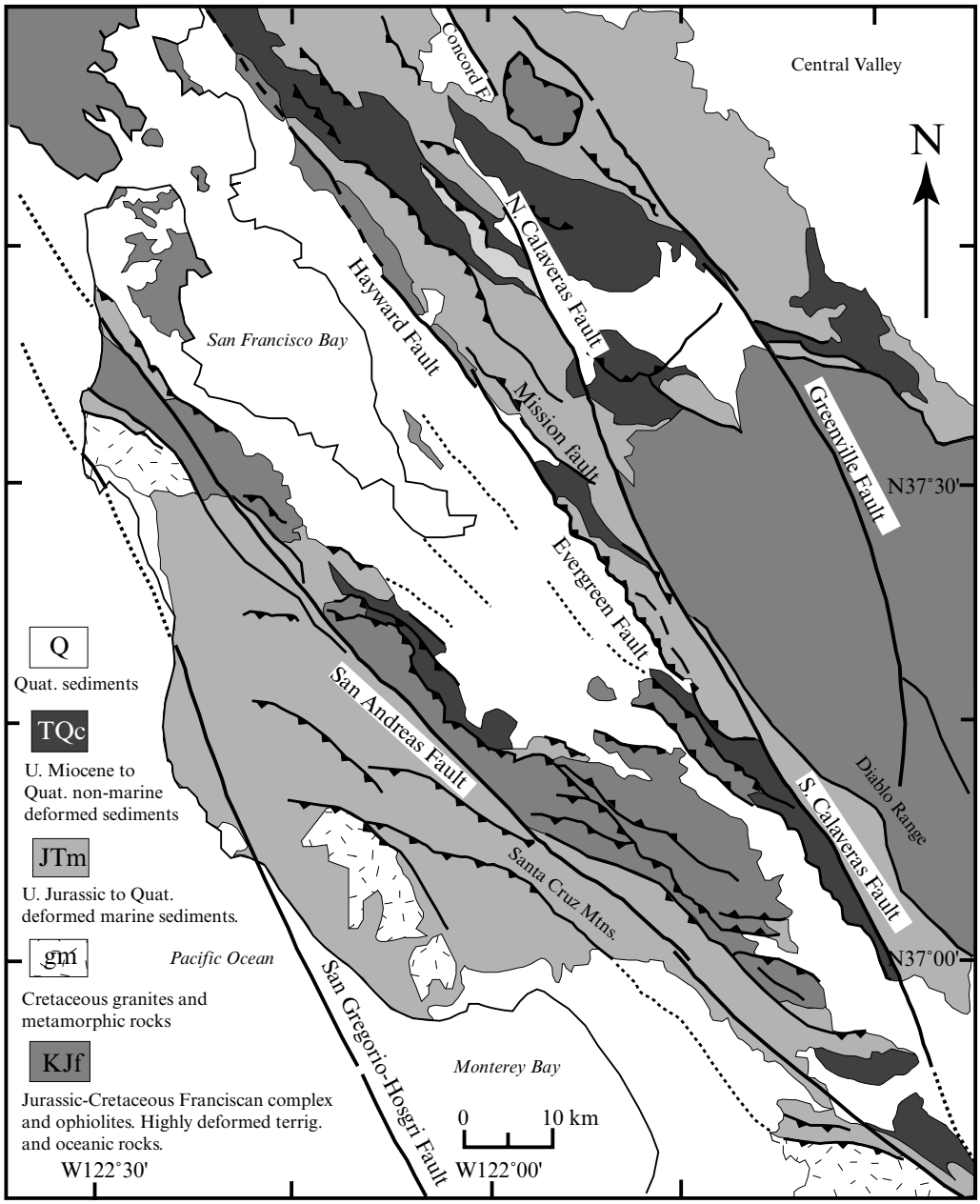

Figure 2. Generalized surficial geologic map of the southern San Francisco Bay region. Heavy lines represent faults, barbs on overthrust block of reverse faults. Simplified map from Aydin and Page (1984).

ger strike-slip events on the Hayward fault (Andrews *et al.*, 1993). However, the lack of dip-slip earthquakes in the area led Andrews *et al.* (1993) to express a need for further investigation and characterization of the region.

A seismic lineament through the Mission Hills appears to link the seismicity on the southern and central Calaveras fault and the Hayward fault (Fig. 1). It originates on the Calaveras fault where the surface trace begins a more northerly strike (Jennings, 1994). The lineament exhibits weak seismicity ($M < 4$) confined to depths of 3 to 8 km and is predominantly dextral strike-slip with little dip-slip movement (Andrews *et al.*, 1993; Wong and Hemphill-Haley, 1992). Transfer of slip between the Calaveras and Hayward faults has been attributed to this lineament (Ellsworth *et al.*, 1982; Wong and Hemphill-Haley, 1992; Andrews *et al.*, 1993), based on the alignment of catalog hypocenter locations from the U.S. Geological Survey (USGS) Northern California Seismic Network (NCSN) with the mapped trace of the Mission fault (Fig. 1). The Calaveras fault south of this juncture is believed to have a long-term slip rate of 15 ± 3 mm/yr (Working Group on California Earthquake Probabilities, 1999). North of the juncture, the long-term slip

rate decreases to 6 ± 2 mm/yr (Kelson *et al.*, 1996), with the remaining slip (9 ± 2 mm/yr) presumably transferred to the Hayward fault (Working Group on California Earthquake Probabilities, 1999, 2003).

Despite the apparent alignment, evidence suggests that the Mission fault is not accomodating deep slip transfer. First, the highest rates of surface creep (8–9 mm/yr observed for several decades before the 1989 Loma Prieta earthquake) on the Hayward fault occur more than 11 km south of the mapped surface expression of the Mission-Hayward fault junction (Lienkaemper *et al.*, 1991; Lienkaemper and Galehouse, 1997) in the Fremont area. Microseismicity is absent vertically below the southernmost Hayward fault where the maximum surface creep rate has been observed (Fig. 1). Another trend of shallow microseismicity diverges from the Calaveras fault south of the Calaveras Reservoir near the town of Alum Rock (Fig. 1) and projects to the southern Hayward fault south of the region of maximum creep. This trend (hereafter called the Alum Rock seismic trend) parallels the Mission seismic trend across the Mission Hills stepover region. The Alum Rock trend is less prominent and has a lower rate of seismicity than the Mission trend. However, no microseismicity occurs directly below the southern Hayward fault north of this trend (Fig. 1). Although this trend projects toward the southern Hayward fault, it is shallow (<5 km depth) and does not connect seismicity on the Hayward fault. Microseismicity is typically associated with creeping faults (i.e., Parkfield segment of the San Andreas fault, southern Calaveras fault, central and northern Hayward fault [Hill *et al.*, 1990]), and aseismic areas are associated with locked fault zones (Oppenheimer *et al.*, 1990; Kafka and Levin, 2001). Therefore, the southern Hayward fault should exhibit microseismicity where it is creeping at 9 mm/yr.

Second, geologic investigations indicate that the Mission fault is a reverse fault (Jones *et al.*, 1994; Graymer *et al.*, 1994, 1995), based on the placement of the older strata over younger strata. Third, Wong and Hemphill-Haley (1992) relocated hypocenters using a 1D velocity model with station corrections and found that the linear trend of seismicity was relocated 1 to 1.5 km southwest of the mapped trace of the Mission fault, dipping steeply to the northeast. Additionally, Wong and Hemphill-Haley (1992) observed that landslide material obscures much of the presumed Mission fault trace and found no evidence of the fault as mapped by Hall (1958) and Dibblee (1980). Wong and Hemphill-Haley (1992) also cite reports of fault trenching by consulting geologists who were unable to identify Holocene activity on the mapped Mission fault. Therefore, they consider the mapped trace of the Mission fault not to be the surface expression of the seismically active structure at depth. They suggest that the observed seismicity is attributable to a Hayward fault with multiple strands: an aseismic trace exposed at the surface along the creeping section and another seismic trace that is not exposed at the surface (Wong and Hemphill-Haley, 1992). Kelson *et al.* (1993) excavated across a tonal lineament and topographic swale that coincides with the surface projection of the relocated seismicity of Wong and Hemphill-Haley (1992) near the Hayward fault but found no evidence for such a structure.

To account for uncertainties in fault location and segmentation, an extension of the southern Hayward fault that projects beyond the Mission trend to the Alum Rock trend has been included as a possible source in earthquake probability studies for the San Francisco Bay area (California Division of Mines and Geology, 1996; Working Group on Northern California Earthquake Probabilities, 1996; Working Group on California Earthquake Probabilities, 1999, 2003). It is critical to understand how slip transfer occurs between the Calaveras and Hayward faults, because understanding the fault connectivity and the mechanism of slip transfer will allow us to better assess the potential seismic hazard, not only from reverse faulting in the stepover region, but from triggered strike-slip faulting on the Hayward fault.

In this article, we attempt to elucidate the subsurface structures that may contribute to the seismic hazard in the Mission Hills. Our investigation uses existing geophysical and geologic data to illuminate the subsurface structure. We develop a 3D *P*-wave velocity (V_p) model for the stepover region from catalog seismicity data of the Northern California Seismic Network (NCSN). Previous studies addressed the crustal velocity and its relation to subsurface structure along the Calaveras fault south of the stepover (Thurber, 1983; Michael, 1988; Dorbath *et al.*, 1996) and the Hayward fault to the north of the stepover (Zhang and Thurber, 2003). Additionally, precise hypocenter relocations using double-difference and waveform cross-correlation techniques have produced more detailed hypocenter relocations, again south of the stepover region (Schaff *et al.*, 2002; Rubin, 2002). Zhang and Thurber (2003) also performed a joint inversion for hypocenters and V_p structure utilizing a double-differencing technique on the Hayward fault, with some overlap with the northern portion of our study area.

We take a broader approach here, combining a 3D V_p model, hypocenter relocations, and focal mechanisms with independent geologic, seismologic, gravity, and aeromagnetic data to develop a structural and kinematic model of the Calaveras-Hayward fault stepover region. Our interpretation suggests a mode of direct slip transfer between the Calaveras and Hayward faults as the Hayward fault splays from the Calaveras fault near the intersection of the Alum Rock seismic trend with the Calaveras fault. A northeasterly dipping Hayward fault diverges from the Calaveras fault, becoming steeper as the fault progresses further north. The Hayward fault separates the San Francisco Bay and Mission Hills blocks, with the San Francisco block wedging under the Mission Hills, causing contraction across the Mission Hills. The Mission fault is internal to the zone of contraction within the Mission Hills. This suggests that the Calaveras and Hayward faults are a single system at seismogenic depths, and this has implications for rupture scenarios used in seismic hazard assessment.

Geologic Setting

Understanding the geologic setting of the region is critical for developing a structural and kinematic model of the region. The Mission Hills rise from the near sea level surface of the East Bay alluvial plain to an altitude of more than 750 m in less than 4 km (Andrews *et al.*, 1993). Uplift of the Mission Hills was coeval with the regional uplift of the California Coast Ranges and is estimated to have commenced ~3.5 Ma (Harbert and Cox, 1989), although Page *et al.* (1998) suggest the present ranges were uplifted after a tectonic pulse about 0.4 Ma. The East Bay Hills and Mission Hills are located between the Calaveras and Hayward faults, and contain numerous contractional structures (reverse faults and folds) in an en echelon arrangement between the major bounding faults (Graymer *et al.*, 1994, 1996; Aydin and Page, 1984). Jones *et al.* (1994) suggest a significant component of vertical displacement on the Mission fault based on a minimum vertical displacement of 520 m of late-Miocene to early-Pliocene rocks.

The surface bedrock geology of the stepover region is representative of fault-bounded, crustal blocks with lithologic assemblages that are largely distinct and easily distinguishable (Fig. 2). The Mission Hills block is composed of Cretaceous and Tertiary marine sedimentary rocks. Also present in the southern part of the stepover region are Franciscan Complex rocks, a subduction zone complex consisting of a mélange of marine sedimentary rocks and ultramafic bodies. These ultramafic bodies include serpentinite blocks of the Coast Range Ophiolite (Graymer *et al.*, 1995, 1996). Alluvial deposits result from erosion of mainly the Franciscan Complex (Graymer *et al.*, 1994, 1995). The northernmost part of the stepover region contains Cretaceous and Tertiary sedimentary rocks of the Great Valley sequence, with blocks of Franciscan Complex concentrated along the Hayward fault zone (Wagner *et al.*, 1990). Mapping of fluvial terraces suggest the Mission Hills is being uplifted at a rate of 1.5 ± 0.5 mm/yr (Kelson *et al.*, 1993).

The Mission Hills block is bounded on the west by the Hayward fault and the adjoining San Francisco Bay block. The San Francisco Bay block is composed of Cretaceous-to-Jurassic Franciscan Complex which is covered by ~250 m of Quaternary alluvium derived from the hills of the stepover region and in most places overlain by two types of interlayered bay deposits (Koltermann and Gorelick, 1992). The base of the Franciscan Complex west of the Hayward fault is estimated at a depth of 15 km and the depth of the Moho below San Francisco Bay is estimated at 25 km (Holbrook *et al.*, 1996). Exposures of Tertiary marine rocks west of the Hayward fault are limited to the western margin of the San Francisco Bay block near the San Andreas fault (Wagner *et al.*, 1990).

Modeling Methodology

We use a standard joint tomographic inversion of *P*-wave travel-time data for V_p and hypocenter locations to image the subsurface structure. We consider the relationship between crustal velocity and rock composition together with the 3D distribution of seismicity to constrain the subsurface location of faults. We then analyze focal mechanisms to evaluate the style of faulting. The results are compared with the local geology and aeromagnetic and gravity data for the region. Combining seismic imaging with complementary information provides a basis for our interpretation of the subsurface geology.

P-wave travel times to local stations from earthquakes, quarry blasts, and seismic refraction shots were inverted for V_p, hypocenter location, and station corrections as described by Thurber (1983) and Eberhart-Phillips and Michael (1998). We use the program SIMULPS12, an algorithm developed by Thurber, Eberhart-Phillips and others (Evans *et al.*, 1994). The data consist of 29,826 *P*-wave arrival times for 576 events from 1984 to 1998, including 477 earthquakes of $M_D \geq 1.5$ in the study region, 49 well-located earthquakes outside the study area, and 61 seismic refraction shots from the BASIX (Brocher *et al.*, 1992) and Morgan Hill studies (Blumling *et al.*, 1985). These events were recorded by 325 seismic stations, including permanent stations of the NCSN and portable stations deployed during seismic refraction studies (Fig. 3). All catalog locations, arrival times, and station information used in the inversion were obtained from the data repository at the Northern California Earthquake Data Center (NCEDC) and the USGS.

The velocity model is defined for nodes in a 3D grid with the *x* axis oriented at an azimuth of 55° (approximately perpendicular to the Mission fault) and the *y* axis oriented at an azimuth of 325° (Fig. 4). The depth spacing of the 3D grid was set at 3-km intervals, whereas horizontal grid spacing varies as shown in Figure 4, to concentrate nodes near the seismic lineaments. We calculate velocity values and hypocenter locations through an iterative, damped, least-squares inversion. Each iteration defines new ray paths, new hypocenter locations, and new V_p values at each grid node. Travel-time residuals showed a linearly increasing positive bias as the source-to-receiver distance increased over 30 km and were significantly positively biased past 70 km. This indicates the model is too coarse beyond the ±15 km from the *y* axis, which affects the travel times for larger source-to-receiver distances. Therefore, we apply distance weighting to each observation, with a source-to-receiver distance less than 30 km given a weight of unity, decreasing linearly to zero from 30 km to 70 km.

We begin with a coarse 3D grid (node spacing >15 km) with *a priori* velocity values at each node from an initial 1D velocity model. The 1D *a priori* V_p model was created with the program VELEST (Kissling, 1995) using *P*-wave arrival times at local stations for 315 earthquakes of M_D 1.5 or greater in the Mission Hills area. These earthquakes occurred between July 1984 and April 1997. We used three different starting velocity models, based on USGS 1D models routinely used for creating earthquake hypocenter catalogs. All three models converged to a similar velocity profile. A com-

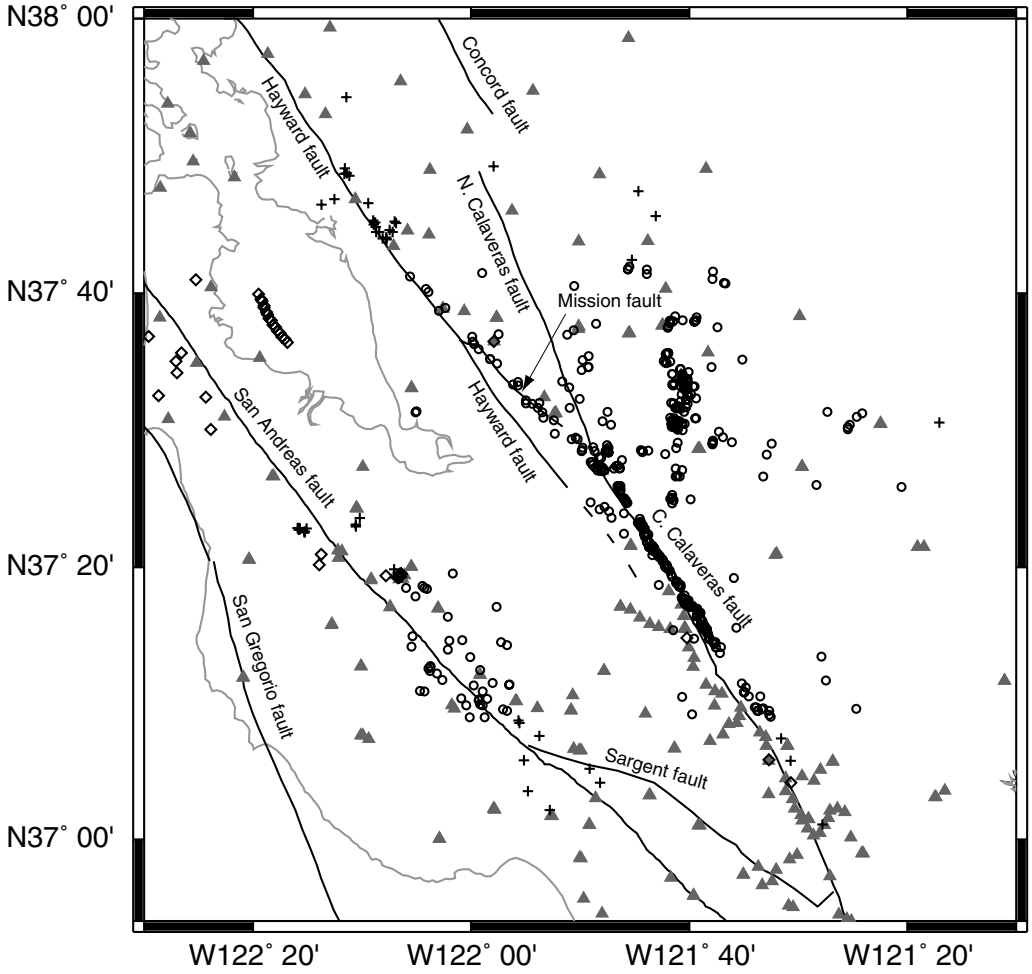

Figure 3. Catalog events used for the fine-model simultaneous inversion. Initial NCSN catalog locations (http://quake.geo.berkeley.edu/ncedc/catalog-search.html) for earthquakes shown by circles. Crosses are well-located events and quarry blasts outside of the region that are considered to be "fixed." Diamonds are seismic survey shots of the BASIX and other experiments. NCSN seismic stations shown by filled triangles. Major seismogenic faults (labeled) represented by heavy black lines.

bined model based on the average convergence model was then used as a starting model to obtain a final, 1D V_p model that was expanded onto a coarse 3D grid for the starting model in the 3D V_p model inversion. The V_p values for the coarse grid were modeled using a series of damping parameters to obtain values for the outer grid nodes of the study area. We gradually increase the model complexity by densifying the grid to the fine model.

Each inversion uses an empirically selected damping parameter that optimizes the trade-off between the data variance and solution variance. The damping parameter is a weighting factor that determines the relative importance given to minimizing the prediction error (or model misfit) or the solution length (or model roughness) (Menke, 1989, pp. 52, 59, 76–79). If the damping parameter is too high, the model is too smooth and details in the structure will be lost. If the damping parameter is too low, the model becomes artificially complex without significantly reducing the data variance. Because the greatest change in the calculated 3D velocity model will occur in the first iteration, we performed a series of single-iteration inversions using different damping values to measure the effect of the damping parameter on the data misfit and solution variance (Fig. 5). For the final model, we selected a damping parameter of 1000, although damping values as low as 400 could be considered acceptable. Because we are attempting to elucidate gross subsurface features, the higher damping value provides sufficient model detail while ensuring a stable inversion.

An inspection of the diagonal elements of the resolution matrix is insufficient to evaluate the model resolution of our damped inversion. The model resolution matrix includes contributions from neighboring nodes, and the off-diagonal elements of the resolution matrix are nonzero. The preferred resolution for a node is represented by a peaked distribution at that node without significant contributions from adjacent nodes. We use the spread function of Michelini and Mc-

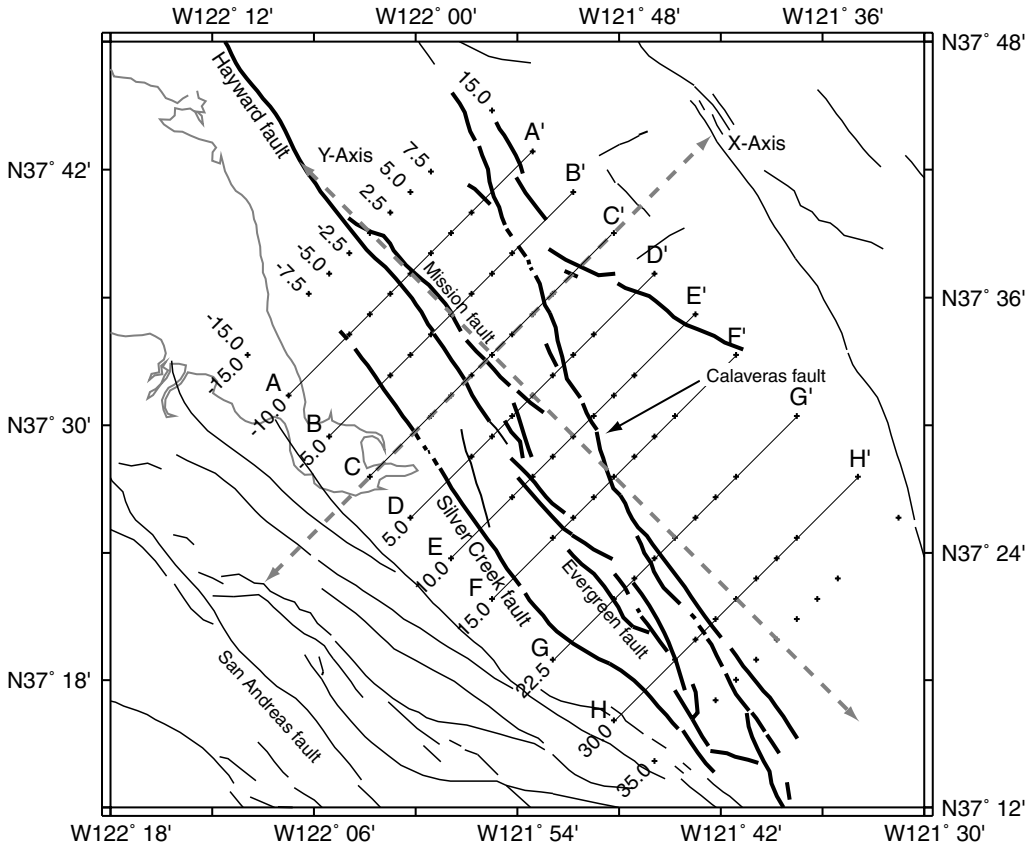

Figure 4. Fine model grid used for inversion. Faults within the model region are represented by heavy black lines. Model *x*-*y* grid points shown by crosses. Grid axes represented by dashed gray lines, with the *x* axis rotated 45° from north. Axis labels are in kilometers.

Evilly (1991) to evaluate the distribution of the resolution matrix. The spread function is calculated for each node from the diagonal element of the resolution matrix and the elements of the corresponding row, weighted by the distance from the node (Michelini and McEvilly, 1991).

Figure 6 shows the model resolution matrix as described by the spread function. This serves two purposes: to evaluate the amount of information in each node and to evaluate the contribution from neighboring nodes. Higher diagonal values of the resolution matrix cause the spread function to be small for the corresponding node. Contributions from neighboring nodes, particularly distant nodes, cause a larger spread function value. As expected, the best resolution occurs in areas where seismicity is more frequent and where the stations are located. The best resolution is in the southern end of the model (spread functions less than 4) between $y = 10$ and $y = 30$ km and is associated with higher rates of seismicity. Although many nodes from 3 to 12 km in depth have a spread function more than 4, the number of modeled ray paths traveling through these nodes typically exceeds 1000. However, the velocities at these nodes have relatively greater contributions from neighboring nodes, reflecting the greater spread function values using the damping value of 1000 and the nonuniform distribution of earthquakes.

Areas with spread function values greater than 8 indicate that the model is poorly resolved in these regions. This typically occurs at shallow depths where station coverage is poor. At shallow depths the rays travel nearly vertically, and the nodes are modeled only where there are stations directly above them. The number of ray paths per node is typically below 50. Similarly, the number of ray paths per node at depths below 12 km is 100 to 500. At depths greater than 10 km, the model also has poor resolution because of limited nodal offsets, and any velocity variations are small because of the higher damping parameter. Below 12 km, the velocity model remains essentially unchanged from the initial 1D model.

Inversion Results

Both the 1D and 3D V_p models provided significant reduction in the data variance. The initial data variance as calculated for the 3D model was 0.043 sec^2. The 1D model with station corrections reduced the variance to 0.0133 sec^2. The final 3D V_p model was obtained after five iterations, with a resulting reduction of the *P*-travel-time variance to 0.033 sec^2, with further reduction in the variance to 0.0123 sec^2 with station corrections. This is an improvement of

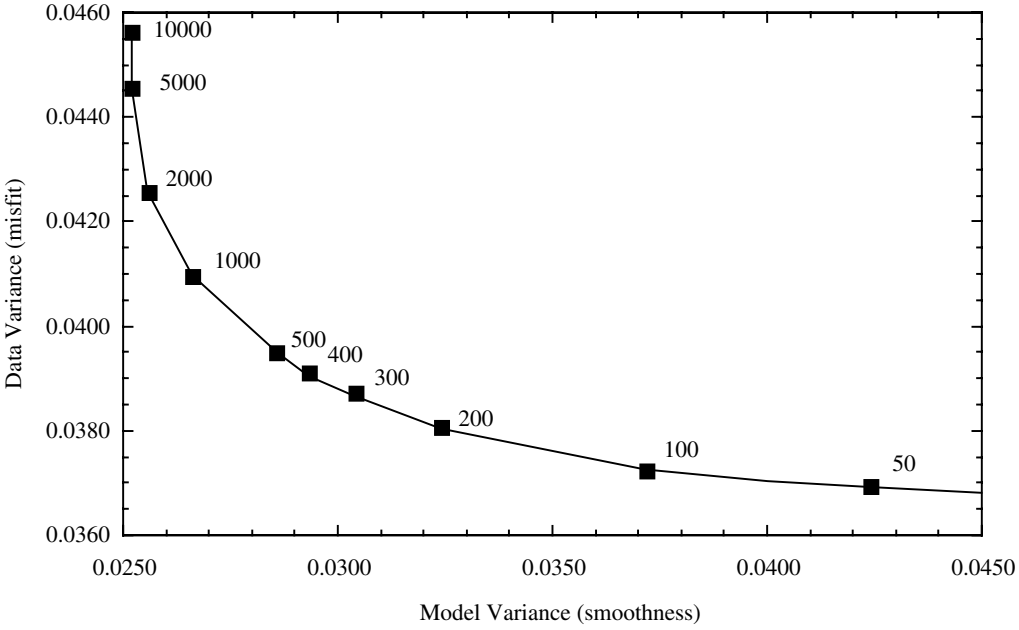

Figure 5. Fine model trade-off curve for various damping parameters (values shown next to graphed points). A damping parameter of 1000 was selected, although values of 400 to 1000 could be considered acceptable choices. The data variance is the weighted sum of the squares of the misfits between the observed and modeled hypocenters normalized by the total weight less the degrees of freedom. The model variance is the sum of the squares of the difference between the velocity nodes and the average velocity divided by the total number of free nodes.

72% over the initial catalog data variance. Although the 3D model provides only an 8% improvement in data variance over the 1D model, the 3D V_p model has the added benefit of providing information about the subsurface structure of the region.

Crustal Velocity Distribution

The final 3D V_p model is shown in Figures 7 and 8. Model contours were obtained from Delauney triangulation of the velocity model nodes. The model reveals lateral velocity variations across the major faults, including a sharp V_p contrast across the Calaveras fault below 3 km depth (Fig. 8B,C,D). The velocity at 3 km depth reaches a relative high near the crest of the Mission Hills in the stepover region (Fig. 7B), conincident with the Mission fault surface trace. High velocities are apparent at depths of 6–9 km in association with the Hayward fault (Fig. 8A–H). North of the Calaveras Reservoir, the velocities are lower to the east of the Calaveras fault (Fig. 8A–E). At the Calaveras Reservoir (Fig. 8F), a relative velocity high is observed at the Calaveras fault. South of profile FF′, the V_p values east of the Calaveras fault are markedly increased over velocities further northward (Fig. 8G,H).

Relocated Hypocenters

The final 3D V_p model with station corrections was used in a simultaneous inversion to relocate the 477 model earthquakes (Fig. 3). For these events, the relative hypocentral relocation errors were 0.015 km (x), 0.220 km (y), and 0.032 km (z). To better characterize the seismicity of the region, we expanded our dataset and relocated 576 events ($M_D > 2$) from January 1978 to July 1998 (Fig. 9). The relative hypocentral relocation errors for these were 0.013 km (x), 0.012 km (y), and 0.032 km (z). The most obvious difference between the NCSN catalog and relocated events appears on the Calaveras fault in the southern portion of the study area. Most of the events used to create the V_p model (all with $M_D > 2$) are located below 6 km. Cross-fault seismicity profiles of this area (Fig. 8G,H) suggest a steep, near-vertical Calaveras fault, in agreement with studies by Michael (1988), Schaff *et al.* (2002), and Rubin (2002) for the Calaveras fault south of our study area. Our relocations are shifted eastward from the surface expression of the Calaveras fault. This may be due to the proximity of these profiles to the fine model boundary.

Separately, we relocate 255 events of $M_D > 1.5$ (some of which were included in the previously mentioned 576 events) for the Mission and Alum Rock seismic trends for 1978–1998 to provide additional information about shallow seismicity, possible sources, and source geometry (Fig. 10). The relative relocation errors for the Mission seismic trend were 0.018 km (x), 0.015 km (y), and 0.044 km (z). The relative relocation errors for the Alum Rock seismic trend were 0.019 km (x), 0.018 km (y), and 0.051 km (z). The

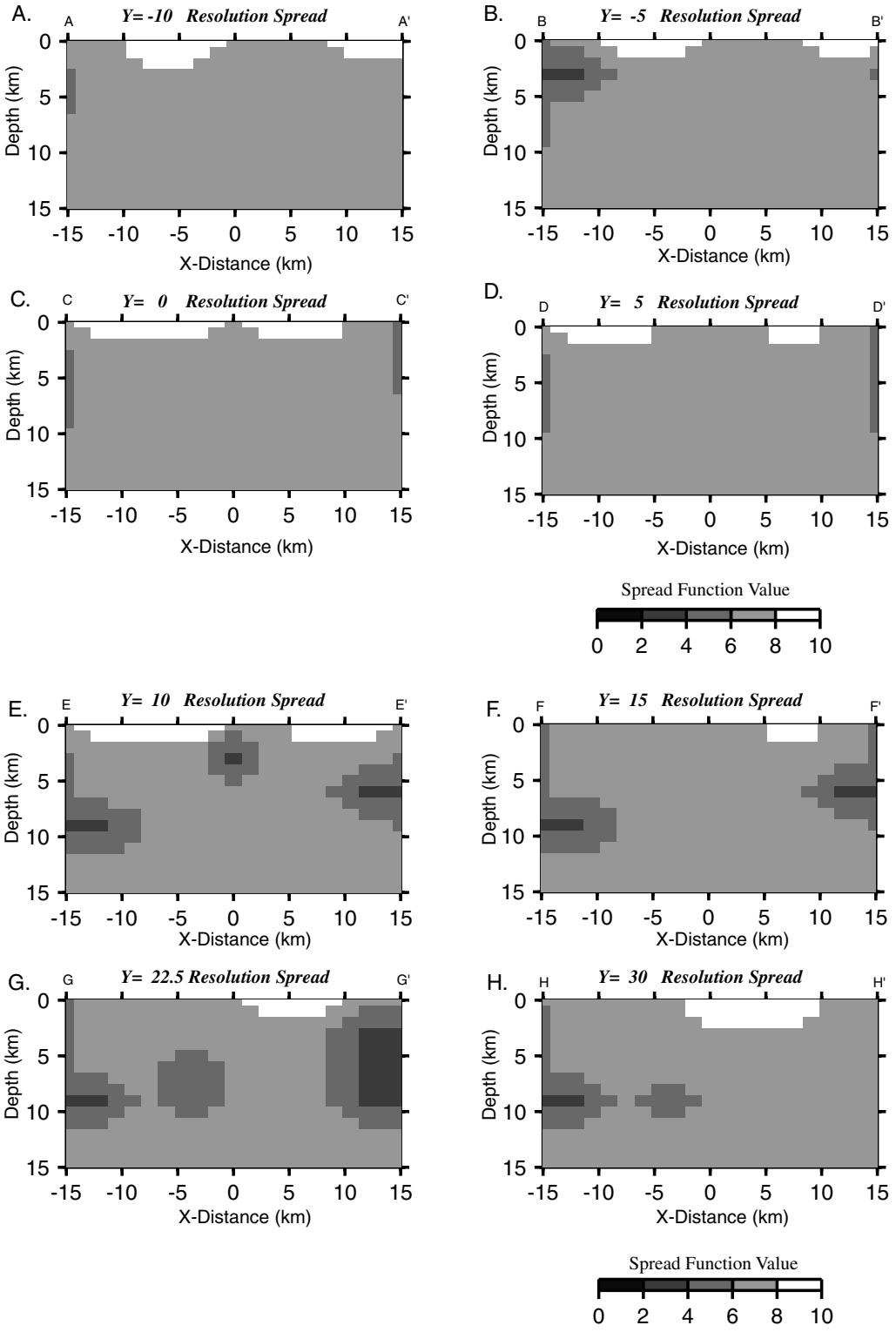

Figure 6. Resolution plots for final model shown in profile view for constant y grid value. The spread function values shown are calculated from the row of the resolution matrix and indicate the degree of smearing in the model. High resolution is reflected in low spread function values. Areas of no resolution or spread greater than 8 are shown in white. Resolution spread for (A) $y = -10$ km; (B) $y = -5$ km; (C) $y = 0$ km; (D) $y = 5$ km; (E) $y = 10$ km; (F) $y = 15$ km; (G) $y = 22.5$ km; and (h) $y = 30$ km.

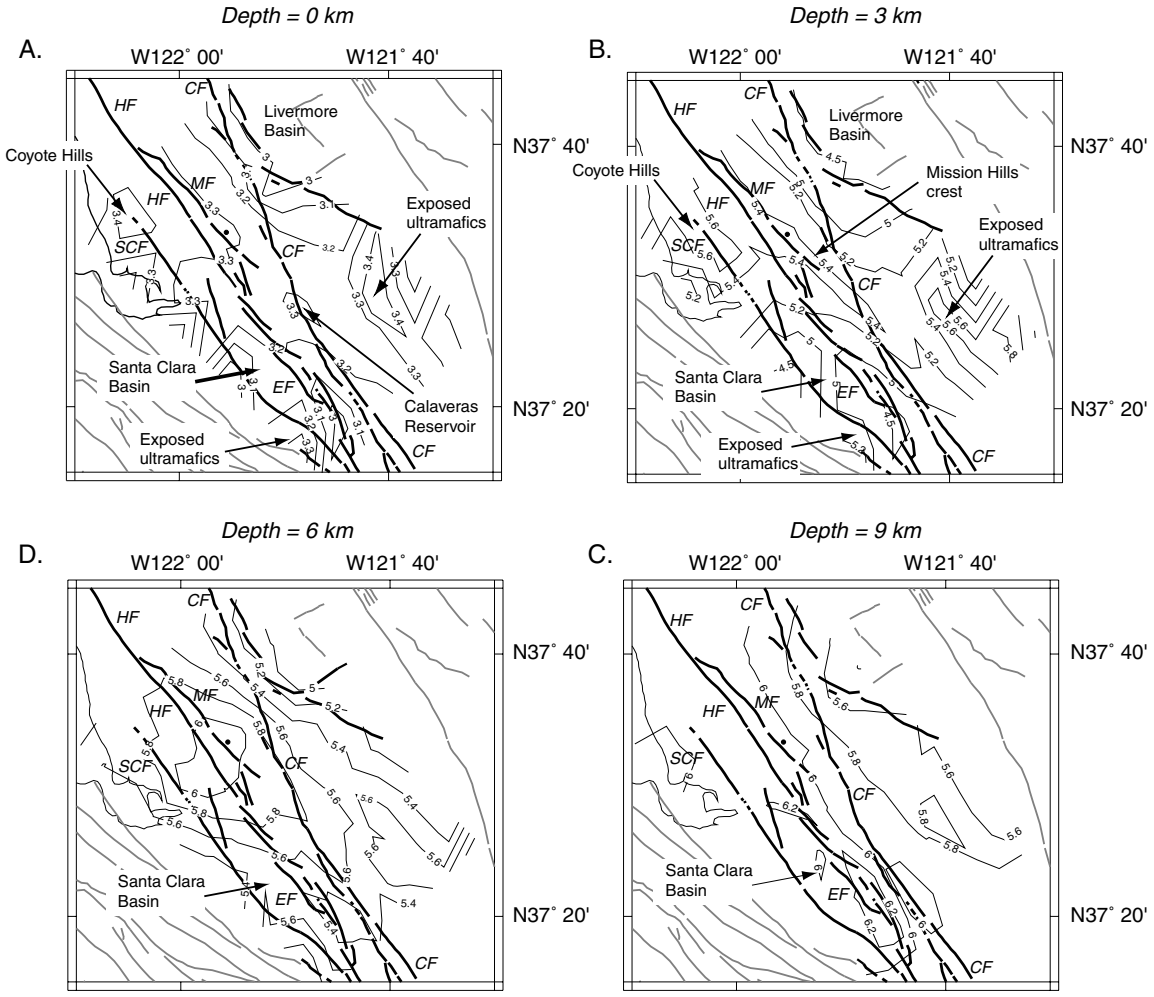

Figure 7. Contour map of V_p model at depth levels of (A) 0 km; (B) 3 km; (C) 6 km; and (D) 9 km. Velocities are in kilometers per second. Prominent geologic features are shown that correspond to general velocity model features. Mapped faults from Jennings (1994) shown as heavy lines, black within and gray outside of the study region. Prominent faults labeled as follows: CF, Calaveras fault; HF, Hayward fault; MF, Mission fault; SCF, Silver Creek fault; EF, Evergreen fault. Velocity contours are from Delauney triangulation of model node velocities.

Figure 8. Cross-sectional plots (profiles of model grid for constant y) of final V_p model, with interpreted subsurface fault structure. Fault locations are based on seismicity, the V_p model, aeromagnetic and gravity profiles, and other supporting geologic data. Dashed, heavy gray lines represent inferred fault locations. Letters above the profiles indicate the surface trace location from Jennings (1994) of the Hayward (H), Mission (M), Calaveras faults (C), Hayward-Evergreen transition (H/E), and Silver Creek fault (SC). Velocity contours are in kilometers per second. Filled circles represent seismicity $M > 2$, projected to planes perpendicular to the y axis of model grid. P-wave velocity models for profiles: (A) $y = -10$ km with seismicity from $-15 < y < -7.5$ km; (B) $Y = -5$ km with seismicity from $-7.5 < y < -2.5$ km; (C) $y = 0$ km with seismicity from $-2.5 < y < 2.5$ km; (D) $y = 5$ km with seismicity from $2.5 < y < 7.5$ km; (E) $y = 10$ km with seismicity from $7.5 < y < 12.5$ km; (F) $y = 15$ km with seismicity from $12.5 < y < 17.5$ km; (G) $y =$; 22.5 km with seismicity from $20 < y < 25$ km; (H) $y = 30$ km with seismicity from $27.5 < y < 31$ km. Velocity contours are from Delauney triangulation of model node velocities.

(*Continued on following two pages.*)

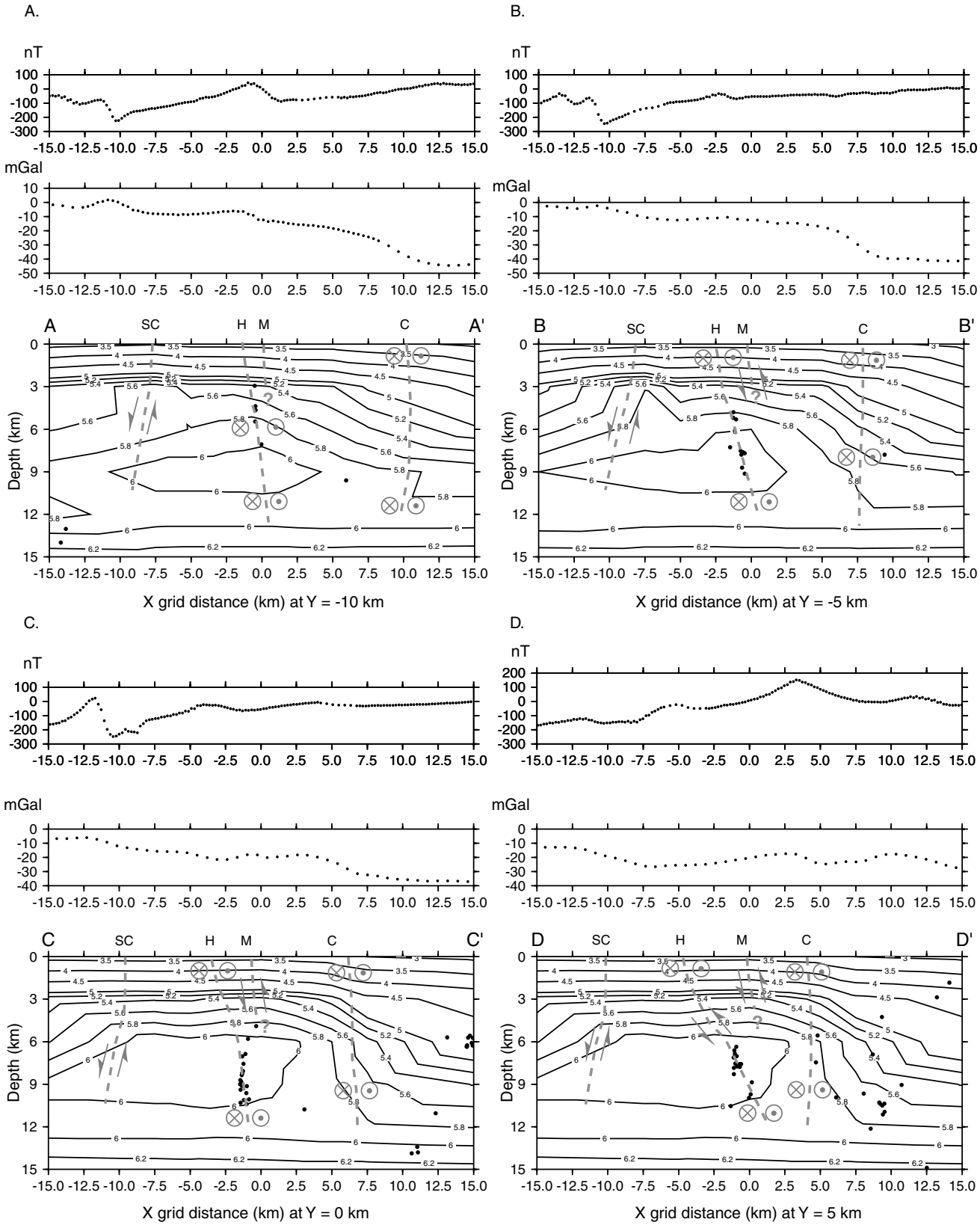

Figure 8. Continued.

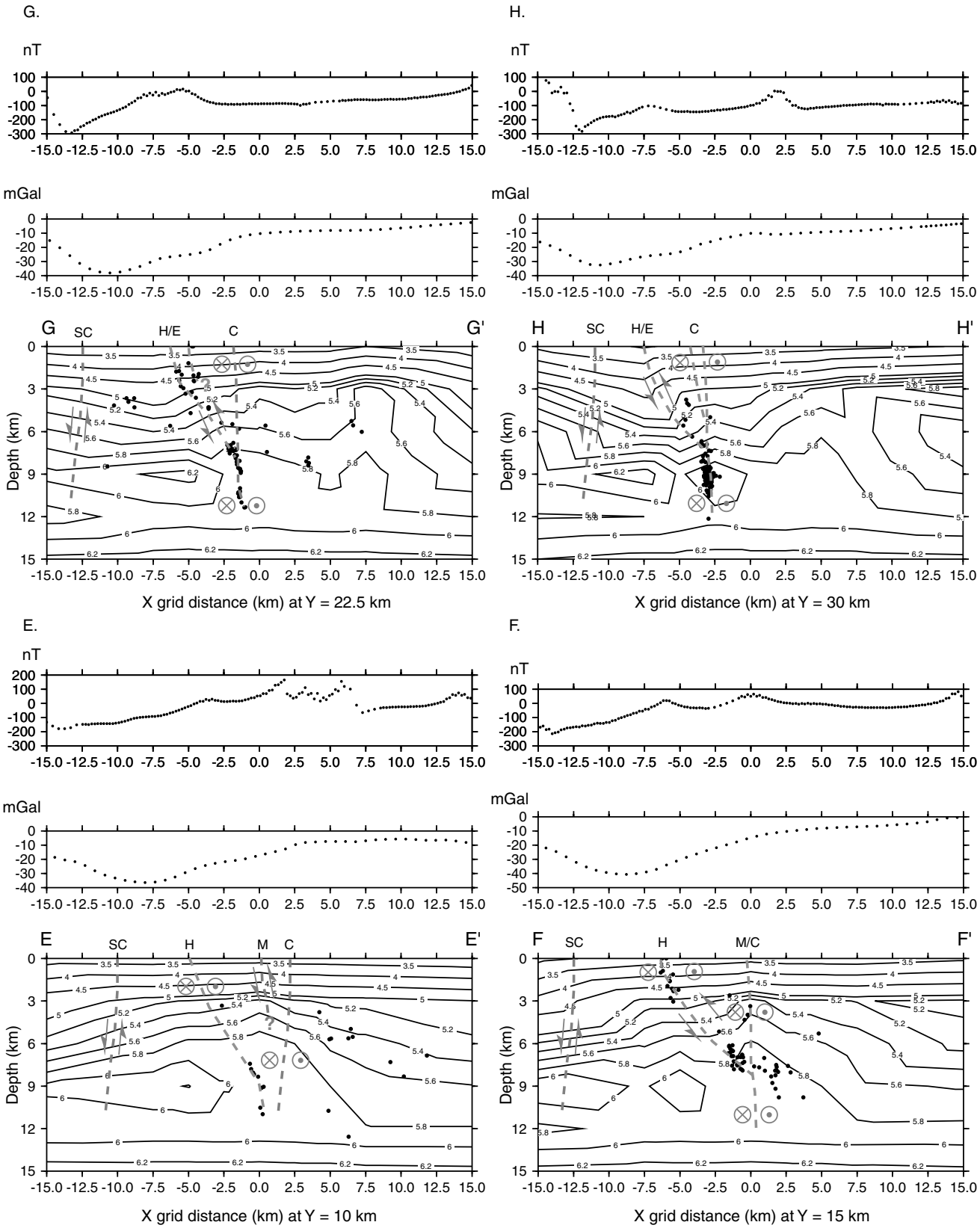

Figure 8. Continued.

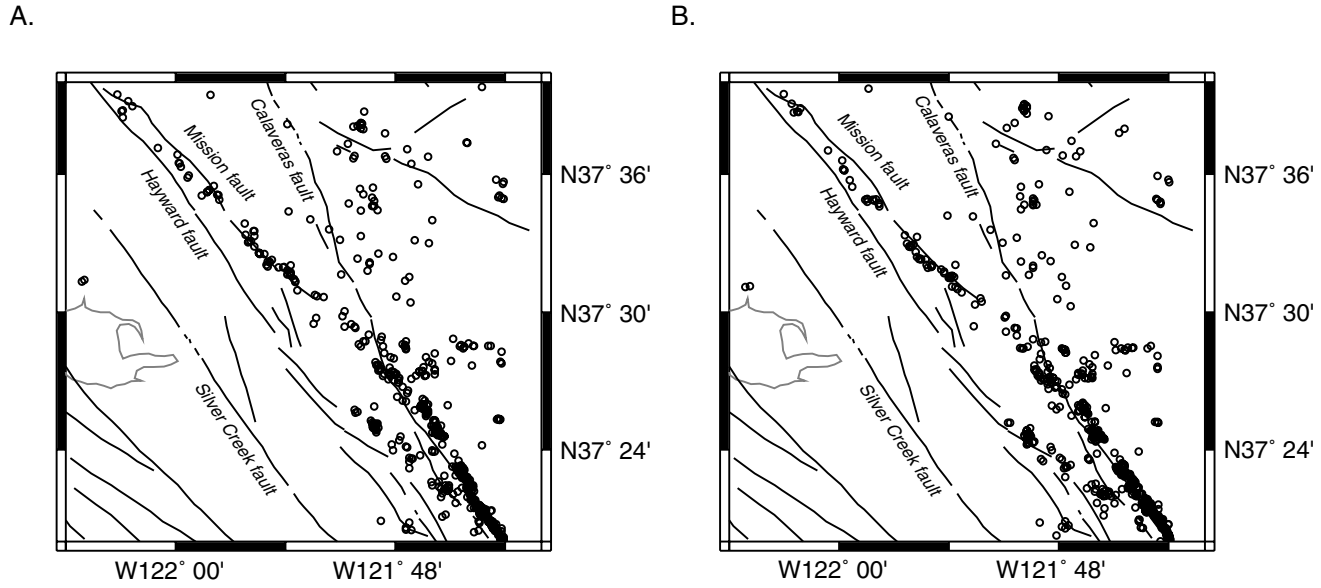

Figure 9. Stepover region $M_D \geq 2$ events from 1978 to 1998. Earthquakes are shown by open circles. Major faults are shown by black lines. (A) Catalog event locations. (B) Relocated events.

relocated Mission trend are shifted southwest of the mapped surface trace of the Mission fault and the NCSN catalog locations by 0.5 to 1.0 km, similar to the relocated trends of Wong and Hemphill-Haley (1992) and Zhang and Thurber (2003).

Seismicity profiles of these trends suggest multiple fault planes as sources. (Ⓔ 3D plots of seismic trends created using LiveGraphics 3D [Kraus, 2003] are included as an electronic supplement to this article, available online at the SSA Web site.) Coordinate axes and hypocenter locations are referenced to the model grid axes shown in Figure 4. Seismicity is typically confined to depths of 3 to 11 km. For the Mission trend, most of the seismicity appears to lie on a single fault plane (Ⓔ Plot is available online at the SSA Web site). The source has a near-vertical dip, with the southern portion of the trend exhibiting a steep northeasterly dip of approximately 70°, with the dip rotating as the trend progresses northwesterly to vertical. The northern end of the Mission trend (Fig. 10B) exhibits clustering at ~5 km and 7 km depth. The central region (Fig. 10C) shows clusters of seismicity at depths of 7 to 11 km. Along the southern end near the junction with the Calaveras fault seismicity (Fig. 10D), the seismicity becomes diffuse, suggesting multiple faults accommodating motion at the junction.

The Alum Rock trend shows two to three clusters of seismicity (Ⓔ Plot is available online at the SSA Web site). This shallow trend (<5 km depth) diverges from the deeper seismicity (>5 km depth) associated with the Calaveras fault. The seismicity (Fig. 10E,F) associated with the Alum Rock seismic trend is more diffuse than the Mission trend. The northern cluster of seismicity (Fig. 10E) forms a distinct linear trend in profile view, with a steep northeasterly dip of ~70°. The southern cluster of the Alum Rock trend (Fig. 10F) shows subset of hypocenters that defines a possible low-angle, eastern-dipping fault. These multiple clusters suggest several fault planes may be responsible for the seismicity of the Alum Rock trend.

Best-Fit Fault Plane, First-Motion Solutions, and Kostrov Summations

To better understand the seismotectonics of the Mission and Alum Rock seismic trends, we calculate both the best-fit fault plane to the hypocenters and first-motion, fault-plane solutions (assuming double-couple) for events on the Mission and Alum Rock seismic trends from 1978 to 1998. We also calculate the Kostrov sum of the moment tensors (Kostrov, 1974). Because the time-span of the data includes the 1984 M_W 6.2 Morgan Hill and 1988 M_W 5.9 Alum Rock earthquakes on the Calaveras fault, there may be concern that these events might not represent the long-term strain mode. However, Oppenheimer *et al.* (1988) found no change in the focal mechanisms near the mainshock rupture before and after the Morgan Hill event, and the orientations of the aftershock slip planes were consistent with orientations predicted by the Coulomb failure criterion due to stress changes from the main shock. Therefore, we believe that the data are representative of the long-term strain orientation in the region.

A potential problem with 3D tomography is the effect that lateral variations in the crustal velocity can have on the modeled ray paths. The velocity contrast across faults at depth may produce lateral refractions, resulting in a systematic bias in the azimuth of the first arrivals. The resulting

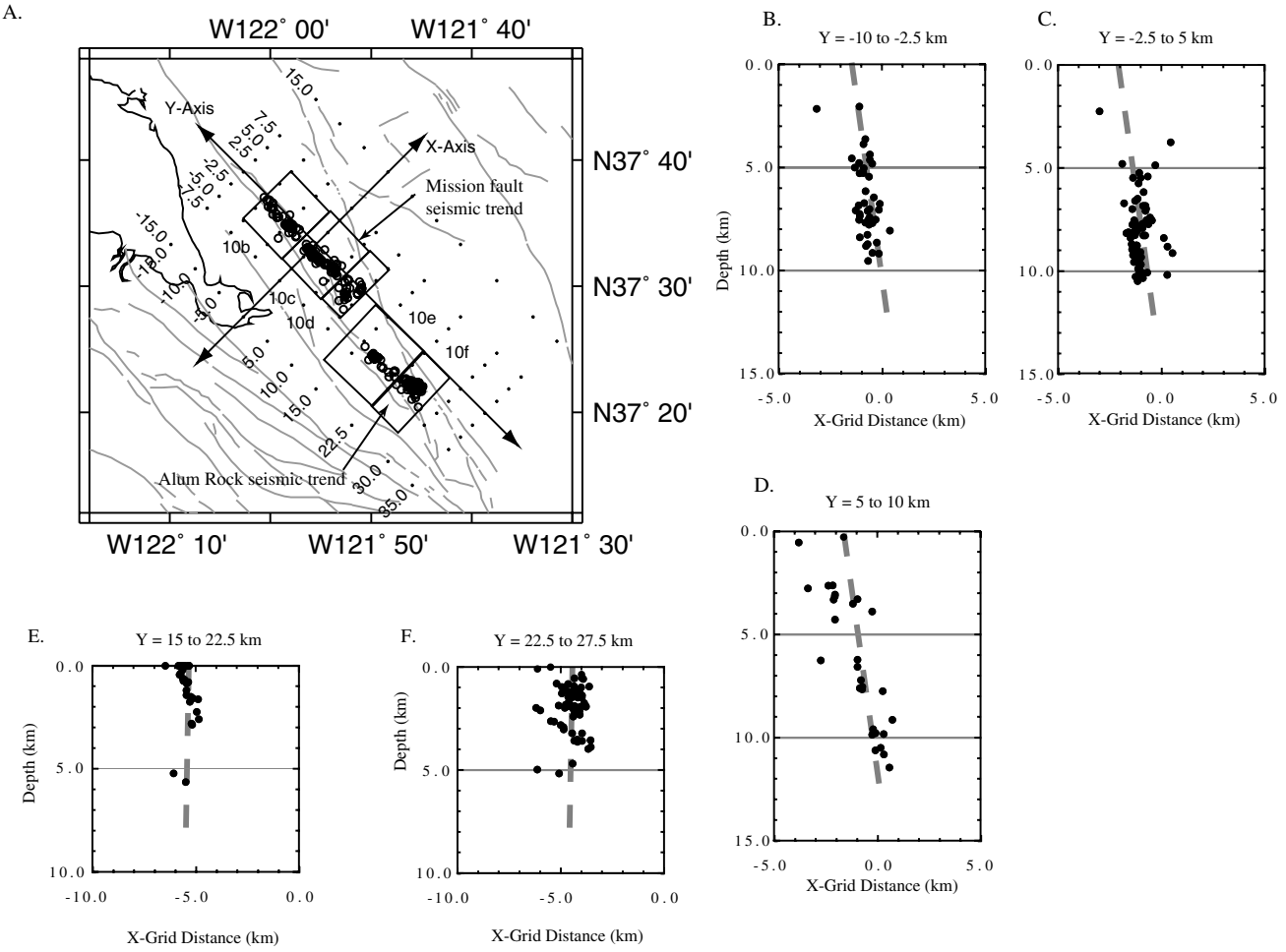

Figure 10. Relocated events on the Mission and Alum Rock seismic trends for the period 1978–1998. All profiles parallel to *x* axis of grid. Dashed gray line indicates the projection of the best-fit fault plane. (A) Map view of events; (B) seismicity profile for events $y = -10$ km to -2.5 km; (C) seismicity profile for events $y = -2.5$ km to 5 km; (D) seismicity profile for events $y = 5$ km to 10 km; (E) seismicity profile for events $y = 15$ km to 22.5 km; (F) seismicity profile for events $y = 22.5$ km to 27.5 km.

incorrectly modeled velocity contrasts will thus introduce bias into the hypocenters. Additionally, ray parameters near the recording stations will be incorrect, resulting in bias in the focal mechanisms. This would be especially true for our modeling, where the use of microseismicity in the modeling places a strong reliance on events with few first motions.

If lateral refractions have introduced a systematic bias, we should observe an abnormally high number of discrepant data close to the fault plane on the "slow" material side. Specifically, higher numbers of discrepant compressive first motions in the slow material's dilation quadrant and discrepant dilations in the slow material's compressive quadrant in a double-couple focal mechanism should be apparent (Dorbath *et al.*, 1996).

To test for lateral refractions, we analyze the distribution of first-motion arrivals by looking at the angle between the ray path and the fault plane. To do this, we calculate the angle between the fault plane and the first arrival ray path, looking at the distribution of discrepant motions from the fault plane for each focal mechanism. We analyzed the distribution of angles between the discrepant motions and the fault plane divided using 15° and 30° bins (Fig. 11). If bias exists, then the distribution of discrepant compressive first motions should peak within 15° to 30° of the azimuth of the fault plane on the "slow" side, and discrepant dilatory first motions should similarly peak near 180° from the fault-strike azimuth. Our analysis of the distributions indicates no such peak in the distribution for both the Mission and Alum Rock seismic trends. Therefore, there is no apparent bias of the relocated hypocenters and focal mechanisms due to lateral refractions.

We calculate the best-fit fault plane for subsets of the relocated hypocenters, using 152 events on the Mission trend and 101 events on the Alum Rock trend. The best-fit fault plane was calculated by taking a sample of the hypocenters and performing a least-squares minimization of the distance

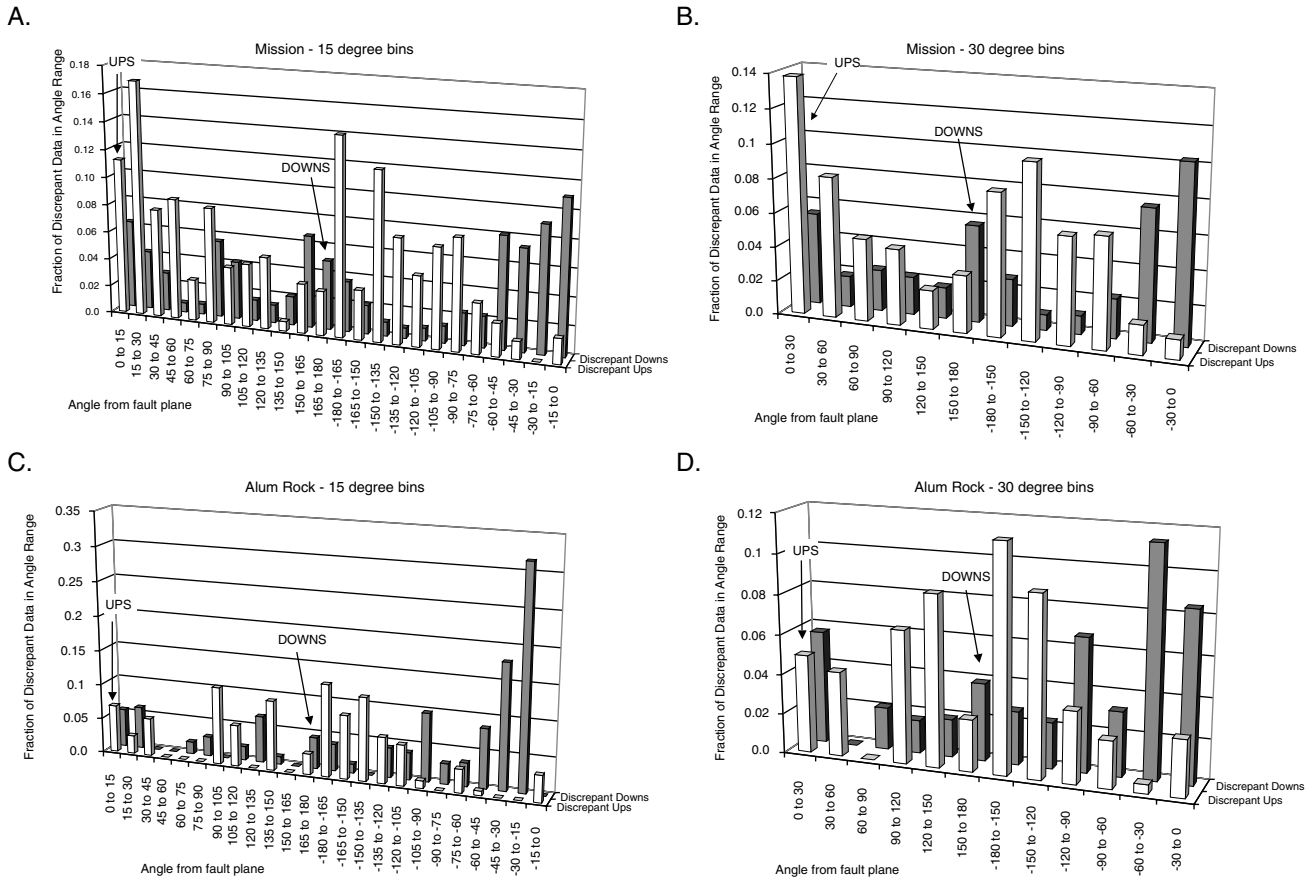

Figure 11. Distribution of discrepant first motions for Mission and Alum Rock seismic trends. Discrepant ups are shown as white columns, downs as gray columns. Distribution of discrepant observations shown for: (A) Mission trend with 15° bins; (B) Mission trend with 30° bins; (C) Alum Rock trend with 15° bins; (D) Alum Rock with 30° bins.

from each hypocenter to a plane. We perform 1000 bootstrap samplings for each data set to calculate the 95% confidence level. The best-fit fault plane for the Mission seismic trend is oriented N43°W dipping 82° to the northeast. The 95% confidence range for the dip angle is 78°–86°, which suggests faulting on a steep northeasterly dipping plane. Although this dip might be due to unmodeled velocity contrasts across the fault, it is in agreement with the dip suggested by the seismicity profiles for the Mission trend (Fig. 10). The best-fit fault plane for the Alum Rock seismic trend is oriented N54°W with a southwest dip of 89°, essentially a vertical fault plane within the uncertainty at the 95% confidence level. However, profiles of the Alum Rock trend suggest that the seismicity is due to multiple fault planes, and therefore the best-fit plane is not fully representative of structures within the trend.

We use the program FPFIT (Reasenberg and Oppenheimer, 1985) to calculate the focal mechanisms for earthquakes relocated with the 3D velocity model. After removing events with less than 20 recorded first arrivals, focal mechanisms for 138 earthquakes from the Mission fault trend and 56 earthquakes from the Alum Rock trends were calculated. An examination of the focal mechanisms shows that the Mission seismic trend is composed of largely strike-slip events, although events with a component of reverse dip-slip motion occur (Figs. 12 and 13). Although seismicity profiles suggest that the northern portion of the Mission trend is likely confined to a single, near-vertical fault plane, the diffuse nature of the seismicity to the south suggests more complexity, with the possibility of multiple, northeasterly dipping structures in a broader fault zone as the seismic source. This is in agreement with the analysis of focal mechanisms by Wong and Hemphill-Haley (1992), who found 19 right-lateral, strike-slip events, 12 reverse events, and 2 normal events in 33 focal mechanisms analyzed. Focal mechanisms for the Alum Rock seismic trend show a combination of strike-slip and oblique-slip events with a significant component of reverse motion (Figs. 12 and 14). Again, the multiple sources suggested by seismicity profiles are evident in the focal mechanisms. The easterly dipping faulting suggested by seismicity profiles and focal mechanisms is in agreement with the general trend of reverse faulting present in this part of the stepover region (Jones *et al.*, 1994).

We determined the average focal mechanism for the

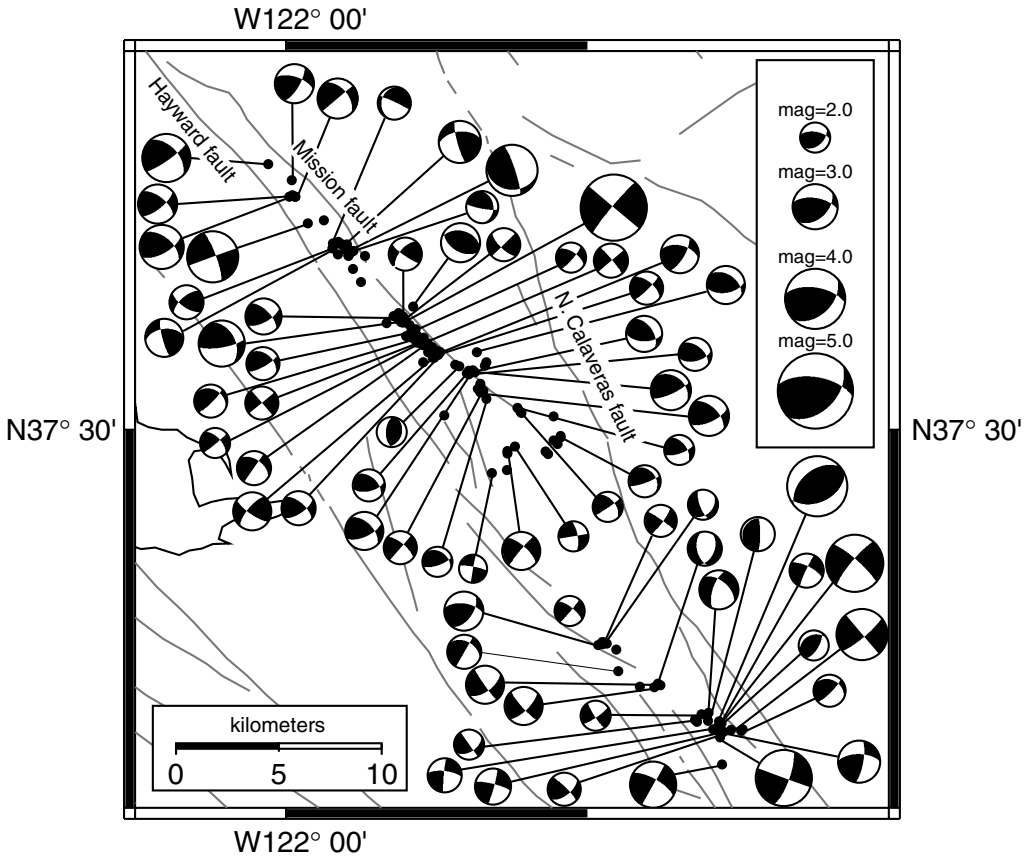

Figure 12. Recomputed focal mechanisms for events $M_D \geq 2$ for the Mission and Alum Rock seismic trends. Mechanisms are lower-hemisphere projections into map view.

Mission and Alum Rock seismic trends with Kostrov moment tensor sums (Fig. 15). Each individual fault plane solution has sufficient uncertainty so that most could be either pure strike-slip events or have a component of dip-slip. This was noted by Andrews *et al.* (1993), who started with the null hypothesis that the events on the Mission seismic trend should be pure strike-slip. By examining each mechanism separately they were unable to void this null hypothesis and concluded that the earthquakes on the Mission trend are pure strike-slip. However, the inability to void the null hypothesis could simply be a result of statistical uncertainty in the focal mechanisms. Additionally, inspection of seismicity profiles indicates that the Mission trend sources may define a more complex zone of faulting. By using the Kostrov sums for the best focal mechanisms, we determine the average mechanism that will have smaller uncertainties to determine whether a statistically significant component of dip-slip occurs in these seismic trends. We can then evaluate the strain release within the volume and determine the dominant style of deformation.

The uncertainty in the Kostrov sum is determined with nonparametric bootstrap statistics, with each data set resampled 1000 times to produce 95% confidence regions. We select the "best" focal mechanisms for Kostrov summation calculations based on the following criteria, presented in the order of selection process: (1) minimum of 20 first arrivals; (2) reject events with misfit greater than 0.15 for the Mission trend and 0.20 for the Alum Rock trend (different misfit levels were applied to the different trends to ensure a sufficient number of events were available for analysis); (3) reject events which, by inspection, have poor coverage of the focal sphere; (4) for multiple solutions, select solution with lowest misfit; and, if the misfit is equal, select solution with fewest discrepant observations. Events with multiple minima that had equal misfit and number of discrepant observations were discarded entirely to prevent bias in the selection process. After reducing the data set, 98 focal mechanisms remained from the Mission trend and 33 focal mechanisms remained from the Alum Rock trend.

We compute the principal strain axes based on the average of 1000 bootstrap samples. The average focal mechanism will have *P, T*, and *B* axes that coincide with the eigenvectors of the summed moment tensors. The bootstrap sampling ensures that the random errors in each mechanism are not propagated through to the calculation of the principal strains, because they are averaged before the eigenvectors are calculated. In the original form, the Kostrov sum is computed by weighting each focal mechanism according to its

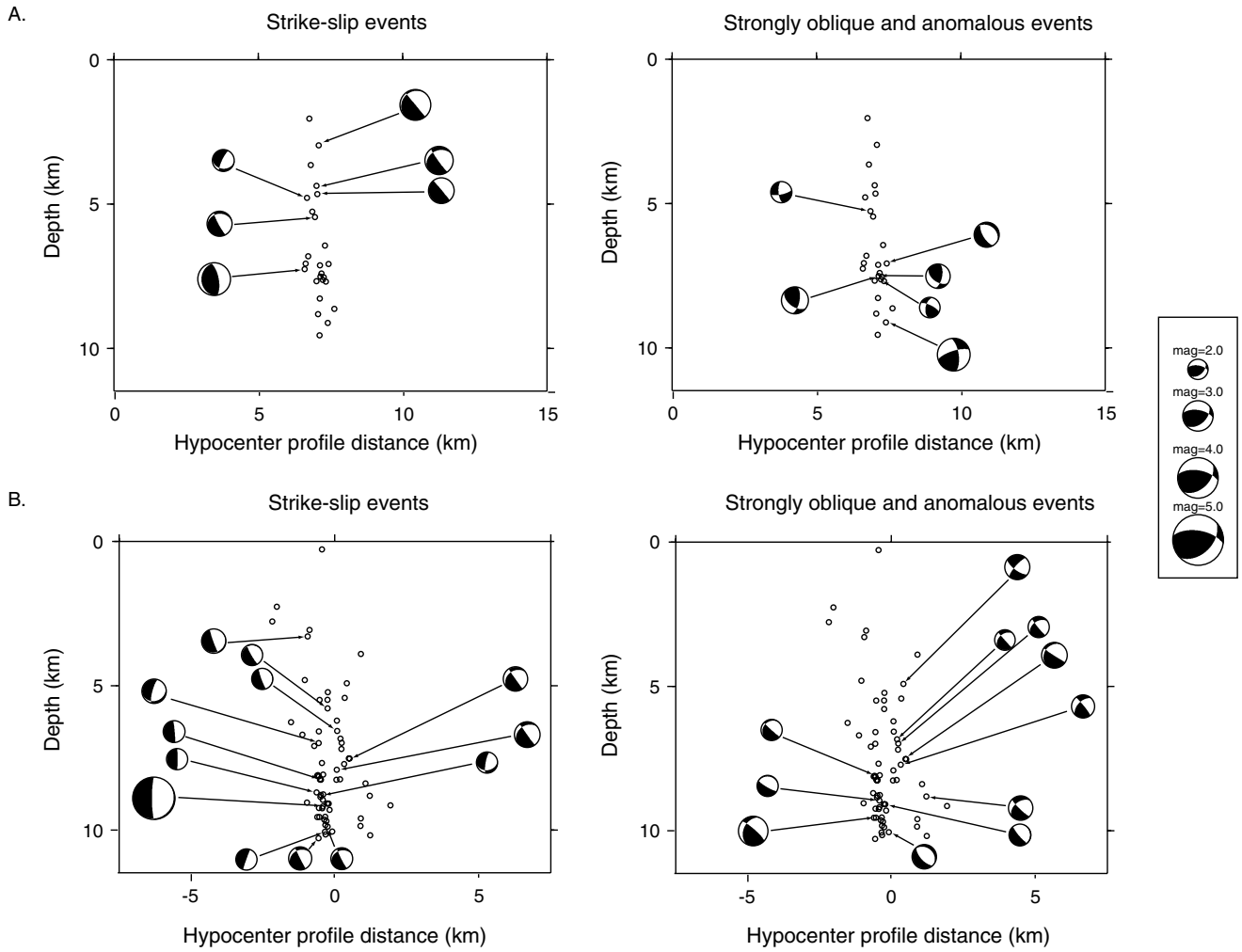

Figure 13. Profile view of recomputed focal mechanisms for events $M_D \geq 2$ on the Mission seismic trend. Focal mechanisms are northwestern-hemisphere projections onto a northeast–southwest vertical plane (parallel to the model grid x axis). Focal mechanisms are divided into strike-slip events and oblique or anomalous (mainly dip-slip) events for the northern cluster of seismicity ($y = -11$ to -2.5 km) (A) and the southern cluster of seismicity ($y = -2.5$ to 10 km) (B).

seismic moment. We performed two sets of calculations for the Kostrov sum. The first calculations weighted the events by a factor of $10^{1.5M}$ (where M is the coda magnitude). As expected, the results were strongly influenced whenever the largest magnitude events were included in the random bootstrap resamplings. Therefore, we also performed a second set of calculations where each mechanism was given equal weight. This reduces the effect of the largest events, whose contribution is heavily dependent on the period studied.

Figure 15 shows the results of the Kostrov sum calculations for the Mission and Alum Rock seismic trends. The Kostrov sum for the Mission seismic trend is indicative of primarily strike-slip motion. The magnitude-weighted solution suggests that the presumed right-lateral component of slip dominates the moment release with almost no reverse motion as a percentage of the total moment released. The equal-weighted solution is right-lateral with a component of dip-slip with reverse motion (northeast side up). Although the Mission trend shows a component of contraction occurring across the region, it is a negligible amount of the total moment released. The Alum Rock seismic trend differs in style from the Mission trend. The magnitude-weighted sum exhibited a consistent trend for the P axis. However there was a considerable range between the T and B axes, due to spread in the focal mechanisms for the largest events in the Alum Rock seismic trend, especially the largest reverse focal mechanism (Fig. 14). Because the first test is weighted by magnitude, the larger events exert more influence on the final P-, B-, and T-axis locations. The resulting orientation for the magnitude-weighted solution indicates primarily reverse-style deformation on a northwest or southerly dipping fault (Fig. 15). The equal-weight solution exhibits a more consistent mechanism of oblique right-lateral slip on a northwest trending, northeast dipping fault. These solutions suggest a

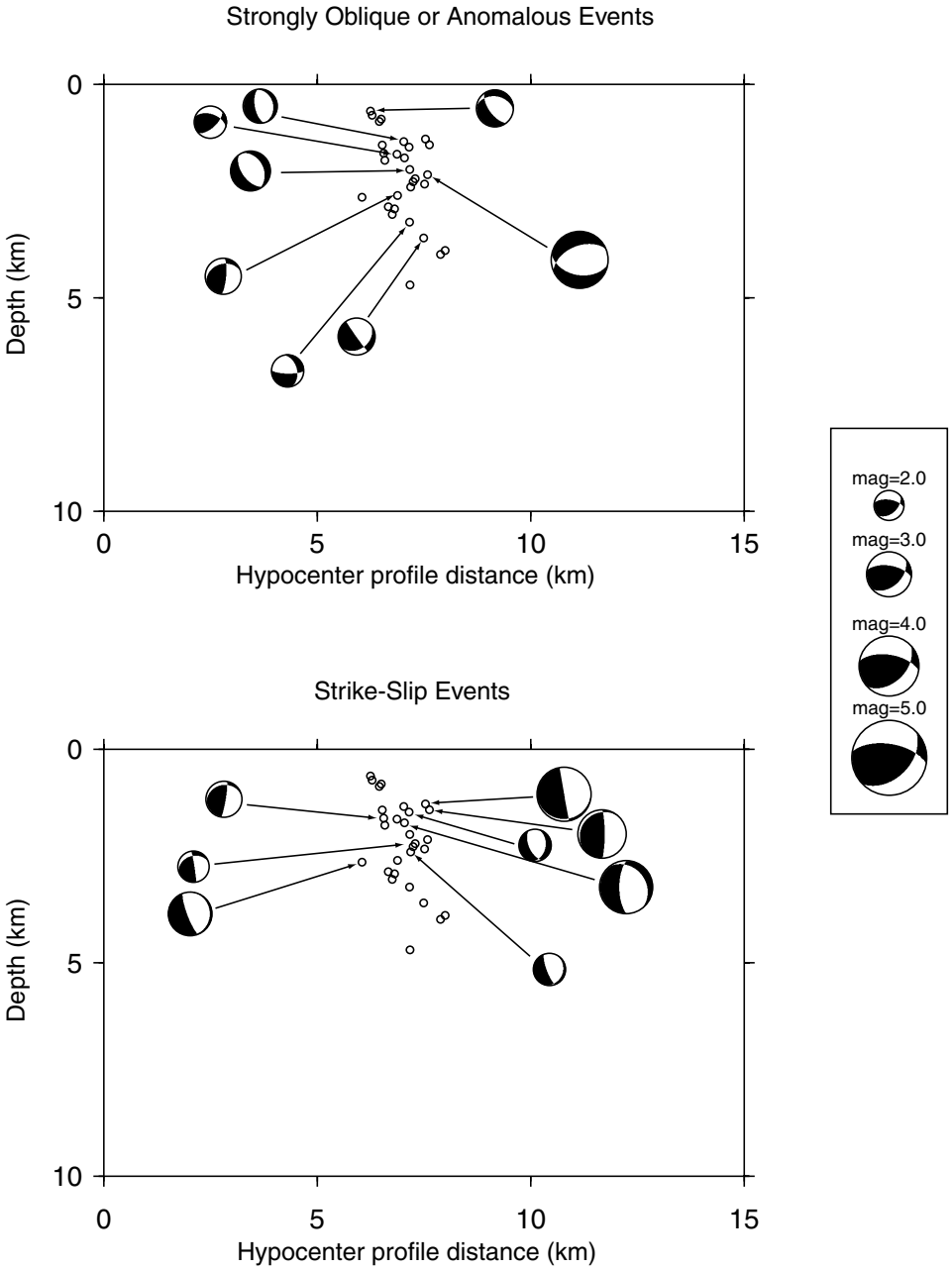

Figure 14. Profile view of recomputed focal mechanisms for events $M_D \geq 2$ on the Alum Rock seismic trend. Focal mechanisms are northwestern-hemisphere projections onto a northeast–southwest vertical plane (parallel to the model grid *x* axis). Focal mechanisms are divided into strike-slip events and oblique or anomalous to the seismic trend.

strong component of contraction across the region in addition to strike-slip motion. This is consistent with the style of faulting observed in the stepover region (Graymer *et al.*, 1995). Based on magnitude-weighted solutions, the Mission seismic trend accommodates mainly strike-slip motion, and the Alum Rock trend is dominated by contraction.

Discussion

Our low-resolution 3D V_p model provides information on the gross subsurface structure and allows for improved hypocentral locations and focal mechanisms. Recognizing that a low-resolution model has limitations, we look for corroborating evidence in other geologic and geophysical data to validate this model. We compare the model with aeromagnetic data (Jachens and Roberts, 1993), isostatic residual gravity data (Roberts and Jachens, 1993), and surface geology (Wagner *et al.*, 1990; Graymer *et al.*, 1994, 1995, 1996). Because V_p is a function of the elastic moduli and density of the material, we make inferences regarding the subsurface composition and structure by combining the 3D

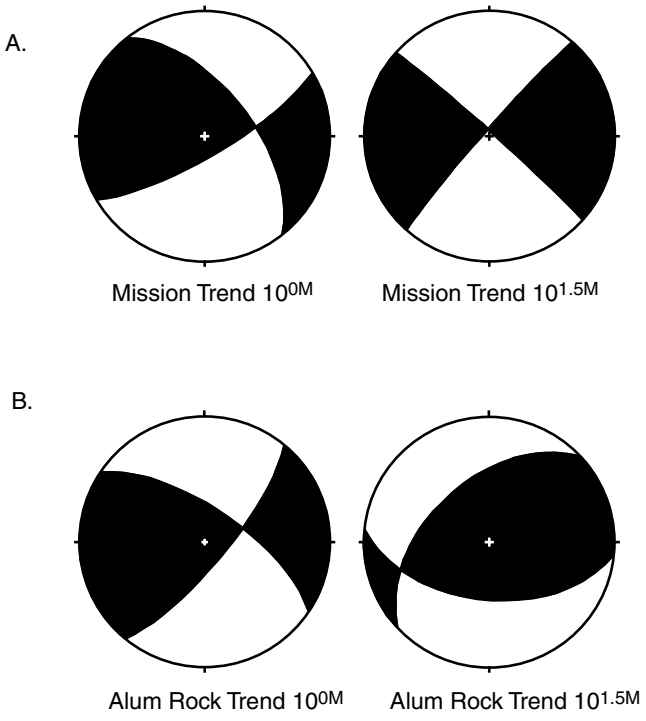

Figure 15. Kostrov sum of the moment tensor inversions for the Mission and Alum Rock seismic trends. A and B show the unweighted and magnitude-weighted average focal mechanism for the Mission and Alum Rock seismic trends, respectively. Kostrov sums were based on 1000 bootstrap inversions for each trend.

V_p model, relocated hypocenters, and focal mechanisms with other geophysical and geologic data.

Certain features of the model that are relatively well resolved based on the model resolution are corroborated by other data (Figs. 7 and 8). A V_p high is visible in sections AA′ and BB′ (Fig. 8A,B) west of the Hayward fault, corresponding to the location of the Coyote Hills. The Coyote Hills define a prominent ridge of low hills, composed of metasedimentary rocks and greenstone of the Franciscan Complex, that project out of the bay alluvial plain west of the Silver Creek fault (Wagner *et al.*, 1990; Graymer *et al.*, 1996). This linear ridge appears as a prominent aeromagnetic low (Jachens and Roberts, 1993) and corresponding local gravity high (Roberts and Jachens, 1993). A relative velocity high on the GG′ section (Fig. 8G) at $x = 7.5$ km corresponds to a magnetic high (Jachens and Roberts, 1993) associated with surface exposure of ultramafic rocks of the Franciscan Complex (Wagner *et al.*, 1990).

Other general features, although not well resolved based on the resolution spread, are also corroborated. The shallow V_p structure at $z = 0$ and 3 km (Fig. 7A,B) shows V_p highs along the Calaveras fault corresponding to the start of a significant negative gradient in the isostatic residual gravity westward toward the San Francisco Bay block (Roberts and Jachens, 1993). Two local V_p lows at $z = 0$ and 3 km correspond with this low-gravity anomaly of the Santa Clara basin (Fig. 7A,B). The gravity low is represented in the velocity profile HH′ (Fig. 8H) between the Evergreen and Silver Creek faults. Additionally, low V_p east of the Calaveras fault at $z = 0$ and 3 km (Figs. 7A,B and 8A–D) correspond with the Livermore Valley basin and the related local isostatic residual gravity low (Roberts and Jachens, 1993). South of the Calaveras Reservoir and east of the Calaveras fault (Figs. 7B and 8G,H), the elevated V_p corresponds to the rocks of the Franciscan Complex in the Diablo Range (Wagner *et al.*, 1990; Graymer *et al.*, 1996), and a relative gravity "plateau" (Roberts and Jachens, 1993).

Although the 3D V_p model is weakly resolved in some areas, there is evidence of discrete blocks of high-velocity material. The profiles of the velocity model with relocated hypocenters show the seismicity clustering around high-velocity regions, suggesting that the material properties of the rock in the fault zone are controlling the distribution of seismicity (Fig. 8G,H). Michael and Eberhart-Phillips (1991) suggested a general relation between increasing V_p and the ability of rocks to accumulate elastic strain energy. They also suggest that if the material properties of the fault zone and the surrounding rocks control how the fault generates earthquakes, then V_p models could be used in fault segmentation models to estimate future seismic moment release (Michael and Eberhart-Phillips, 1991). Regions of relatively high velocity correspond to local aeromagnetic highs (Jachens and Roberts, 1993) and suggest the presence of ultramafic rocks in the fault zone. Ultramafic rocks are exposed at the surface along the Calaveras and Hayward faults (Wagner *et al.*, 1990; Graymer *et al.*, 1994). Control of seismicity by these ultramafic bodies has been observed further northward on the Hayward fault, where seismicity is concentrated on the western side of the San Leandro gabbro body (Ponce *et al.*, 2003).

Development of Structural Model

The uplift in the Mission Hills region has been attributed to local fault geometry or the partitioning of the contractional strain from the oblique motion along the Pacific-North American Plate boundary. Aydin and Page (1984) examined the East Bay and Mission Hills and concluded that the left stepover geometry of the right-lateral Calaveras and Hayward faults resulted in contractional strain in the region between them. Jones *et al.* (1994) argue that the observed reverse faulting and folding in the region is caused by an eastward translation of crustal blocks that move along a mid-crustal decollemont at 12–15 km depth, allowing tectonic wedges to translate eastward and accounting for the compressive component of the oblique motion of the Pacific plate. It has been proposed that the transfer of slip between the Calaveras and Hayward faults occurs on this subhorizontal ductile shear zone (Jones *et al.*, 1994). This is difficult to substantiate without additional evidence of the subsurface geology and fault geometry at greater depth. However, seis-

mic reflection studies suggest that the northern Hayward and San Andreas faults are dipping structures and continue below this speculated detachment (Parsons and Hart, 1999). Therefore, we do not believe that a detachment is responsible for slip transfer, and we base our model on the stepover scenario of Aydin and Page (1984).

Fault stepover regions and similar fault discontinuities in strike-slip faults show that left-stepping, dextral-slip systems produce regions of convergence in the stepover region (McClay and Bonora, 2001; Westaway, 1995; Twiss and Moores, 1992, pp. 117–124; Woodcock and Fischer, 1986; Christie-Blick and Biddle, 1985). This geometry produces a strike-slip duplex, a region of deformation bounded by major faults containing horses separated by internal faults that accommodate strike-slip and vertical motion. The region bounded by the major faults experiences internal deformation through folding and faulting to accommodate the convergence. However, the Calaveras-Hayward fault stepover is not a "pure" stepover, because the Calaveras fault continues to slip north of the Mission Hills. Despite this, the fault geometry will produce a similar zone of convergence (Aydin and Page, 1984) and is structurally similar to a contractional duplex.

Based on the fault geometry, geologic and geophysical evidence, and the results of our velocity model with relocated hypocenters, we suggest that uplift in the Mission Hills region is caused by the San Francisco Bay block wedging under the Diablo Range, with relatively high-velocity material (and by inference, strong and difficult to deform) translating along the fault. As the wedge proceeds northwesterly along the Calaveras fault, the block boundary also moves northward. This tectonic "snow plow" of Franciscan Complex rocks west of the Calaveras fault is being driven under the Mission Hills as the block translates to the northwest. This hypothesis implies that the Hayward-Evergreen fault system is a bounding fault along the face of the contractional strike-slip stepover, because the block to the southwest of the fault is wedging under the Mission Hills. A corollary is that the Hayward fault may also be the site of reverse motion, with the Mission Hills representing the hanging wall. Koltermann and Gorelick (1992) and Jones *et al.* (1994) report 225 m and 300 m, respectively, of vertical displacement across the Hayward fault in the Mission Hills area. As a southern extension of the Hayward fault, the Evergreen fault serves as the direct interface between the leading edge of the wedge of the contractional stepover. A similar fault structure is observed further south, where the San Andreas fault makes a slight westerly jog and the Paicines-Calaveras faults diverge near San Juan Bautista (Dorbath *et al.*, 1996).

In Figure 16, we compare our model interpretation with analog models of restraining stepovers in strike-slip fault systems from McClay and Bonora (2001). The southern and central Calaveras fault exhibits ~15 mm/yr, of which 9 mm/yr of slip is believed to be transferred to the Hayward fault, leaving the northern Calaveras fault to slip at 6 mm/yr for another 40 km further north from the where the Mission seismic trend diverges from the Calaveras fault microseismicity (Working Group on California Earthquake Probabilities, 1999). Despite this added complexity of incomplete slip transfer, similarities in structure are observed, suggesting that the stepover analogy is suitable. In Figure 16, the bounding fault on the left side of the analog model of McClay and Bonora (2001) represents the Hayward-Evergreen fault system. The bounding fault splays from the analog model's main fault trace, which represents the Calaveras fault (Fig. 16, analog profile A). The bounding fault accommodates both strike-slip and dip-slip movement (Fig. 16, analog profiles A and B) and bounds an area of uplift within the Calaveras-Hayward system. As the fault system progresses further north (Fig. 16, from analog profiles B to D), more strike-slip movement is accommodated by the bounding fault and the faults within the analog model exhibit strike-slip and vertical slip. Our interpretation of the V_p model and microseismicity places the shallow seismicity of the Alum Rock trend on the dipping surface of the bounding fault. However it is likely a broad fault zone with deformation distributed among several faults. The Mission fault is represented in the analog model as one of the prominent internal faults contained by the bounding faults. Strike-slip movement is present on the Mission fault equivalent in the analog model, due to shear within the duplex structure. Our V_p model and microseismicity interpretation places the deeper seismicity of the Mission trend on the bounding Hayward fault at the northern end, while the shallow events occur on the Mission fault. Our model interpretation suggests a steeper dip to the Hayward fault than the bounding fault of the analog model, as well as a closer distance between the Hayward and Mission faults than the corresponding faults in the analog model. These differences in the fault geometry between the analog model and the Calaveras-Hayward system may be due to the incomplete nature of the restraining stepover and continuation of slip on the northern Calaveras fault. Slip transfer is completed to the left-bounding fault and the faults internal to the contractional stepover merge with the bounding fault (Fig. 16, analog profile E), as represented by the convergence between the Mission and Hayward faults.

Model Implications

Our structural and kinematic model combines a 3D V_p model, relocated hypocenters, and recomputed focal mechanisms with independent geologic and geophysical data. In particular, our model provides for a mechanism of slip transfer between the Calaveras and Hayward faults. The Mission and Alum Rock seismic trends reflect the style of deformation and kinematics of the region. These seismic lineaments exist in an area of active contraction, exhibiting predominantly strike-slip motion but with a clear component of vertical deformation. The seismic lineaments are arranged en echelon, parallel to the en echelon arrangement of mapped reverse faults and folds in the area (Graymer *et al.*, 1994,

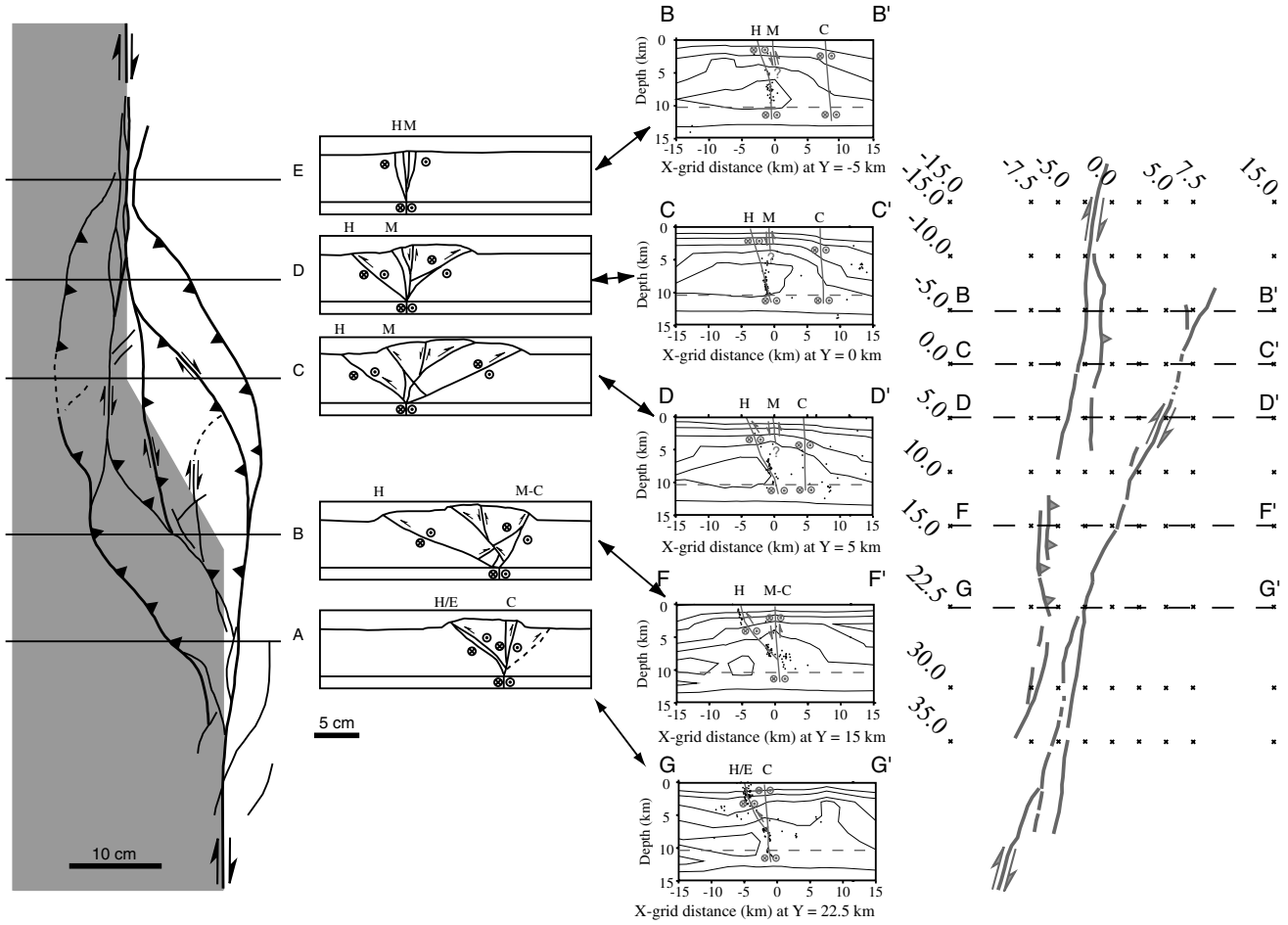

Figure 16. Comparison of the V_p model and relocated hypocenters with the analog model of a restraining stepover of McClay and Bonora (2001). Relative slip motion indicated. Model faults are indicated by H, Hayward fault; M, Mission fault; C, Calaveras fault. The analog model shown is a reflection image of the original left-lateral model of McClay and Bonora (2001). Note the left-bounding fault in the analog model, which is analogous to the Hayward fault system, accommodates both reverse and strike-slip motion.

1995; Jones *et al.*, 1994). Andrews *et al.* (1993) suggest that strike-slip and dip-slip motion are partitioned onto two (or more) discrete fault surfaces, and that the dip-slip surface is locked while the strike-slip surface exhibits microseismicity. Our analyses suggest a single fault zone responsible for the Mission trend, with the hypocenters on the northern part of the Mission trend less dispersed than in the south near the Calaveras Reservoir (Ⓔ plot is available online at the SSA Web site). The fault planes are near vertical to steeply northeasterly dipping (Figs. 10 and 13). The focal mechanisms for these relocated events suggest that most of the observed dip-slip motion occurs during oblique strike-slip events. No seismicity is associated with pure thrust faulting, so we cannot directly support or disprove a large dip-slip fault of significant seismic potential in proximity to the Mission fault. The focal mechanisms also suggest the possibility of multiple sources, confined to a relatively narrow fault zone.

The Alum Rock trend is more dispersed than the Mission trend. Three discrete groupings of seismicity are evident in hypocenter profiles (Ⓔ available online at the SSA Web site). The northern part of the trend is shallow and defines a northeasterly dipping plane. The southern part of the trend contains two discrete clusters: one cluster that defines a northeasterly dipping plane, and another that is a diffuse, globular cluster with no apparent fault plane. Focal mechanisms for events $M_D \geq 2$ show primarily strike-slip behavior, although some reverse and normal events are indicated (Figs. 12 and 14). The wide range of behavior observed in the focal mechanisms for the Alum Rock trend also suggests that strain is distributed on multiple fault planes and in a manner that is more widely dispersed than the Mission trend.

The Mission Fault, Mission Seismic Trend, and Slip Transfer. We believe that the Mission fault is not the mechanism of deep slip transfer between the Calaveras and Hayward faults. The primary evidence for this is that the

Hayward fault exhibits surface creep at 9 mm/yr, its highest rate observed along its surface trace, ~11 km south of the junction between the surface traces of the Mission and Hayward faults (Lienkaemper, 1992; Lienkaemper and Galehouse, 1997; Graymer *et al.*, 1994). Therefore, slip transfer between the Calaveras and Hayward faults likely occurs south of the Mission-Hayward fault junction. Relocated hypocenters of the Mission trend lie southwest of the mapped trace and show a steep dip to the northeast, in agreement with relocations performed by Wong and Hemphill-Haley (1992) and Zhang and Thurber (2003). If these relocations are accurate to <500 m, then the seismicity would have to dip southwest for the seismicity to project back to the surface trace of the Mission fault. Studies of convergent regions associated with strike-slip faulting suggest that the Mission fault should be a steeply northeasterly dipping reverse fault (Aydin and Page, 1984; Woodcock and Fischer, 1986). Therefore, we believe that the Mission fault is not the source of the Mission seismic trend. However, the Mission fault likely accommodates deformation within the contractional region.

The velocity model indicates a velocity contrast (Fig. 8B–F) across the Mission seismic trend, delineating a significant structure that bounds contrasting crustal blocks. Although our velocity model resolution is low and the exact boundaries imprecise using the velocity model alone, we can combine the seismicity and the velocity model to infer the subsurface structure. We interpret this structure as the Hayward fault, which is the eastern boundary of the San Francisco Bay block. Slip transfer is accommodated as the Hayward fault diverges from the Calaveras fault. Near the junction of their surface traces, the Mission fault may merge into the Hayward fault at depth and diverge southward until it reaches the Calaveras fault at the Calaveras Reservoir.

Figure 8 shows the proposed subsurface fault architecture of our model. We propose that the southern Hayward-Evergreen fault system is seismically active and that the southern Hayward fault is a steeply dipping fault that extends from the surface through the upper crust. The Hayward fault diverges from the Calaveras fault, providing a mechanism for the direct transfer of deep slip. As the Hayward fault begins to diverge, it deepens and steepens to the north, and the hypocenters diverge from the Calaveras fault onto the Mission trend. In this model, the Mission fault is an oblique-slip fault that accommodates some of the internal deformation in the stepover region. Although our interpretation places the Mission trend on the Hayward fault, the Mission fault is not precluded as a source of some of the events due to the hypocenter uncertainties. However, the full breadth of geologic and geophysical evidence suggests otherwise. It is unlikely that the Hayward fault, exhibiting surface creep at its maximum rate of 9 mm/yr, is slipping without microseismicity at depth, especially in an area of contraction. Although shallow slip and surface creep is observed where the Hayward fault is locked at depth further northward, the rate of slip is considerably less than the deeper loading rates (Lienkaemper and Galehouse, 1997; Bürgmann *et al.*, 2000; Simpson *et al.*, 2001). Additionally, the distribution of microseismicity on the Mission trend is suggestive of fault creep, yet no creep has been observed on the Mission fault (Wong and Hemphill-Haley, 1992).

Seismic, geodetic, and geologic data require that most of the strain release in the San Andreas fault system within the San Francisco Bay region occur on vertical strike-slip faults. However, strain release within the San Andreas fault system can also be accommodated by pure or oblique strike-slip motion on dipping planes, and a steeply dipping Hayward fault zone that splays off of the Calaveras fault can accommodate both strike slip and oblique slip (Fig. 8).

The Role of the Alum Rock Trend. The Alum Rock seismic trend is more enigmatic and the role it plays in slip transfer is unknown. Profile views of seismicity distribution show that the Alum Rock trend is largely confined to depths of ~5 km or less (Fig. 14). A subset of the seismicity in profile view suggests a shallowly dipping fault surface, perhaps on fault splay (Fig. 14). For all the events, the "best-fit" fault plane was nearly vertical. The average focal mechanism, however, suggests that appreciable shortening is occurring along the Alum Rock seismic trend (Fig. 15). Because the seismicity is largely shallow, these events are likely evidence of distributed contractional strain through multiple smaller faults in a broad Hayward fault transition zone.

Implications for Seismic Hazard. Our structural model has implications for the seismic hazards in the southern San Francisco Bay region. If the southern Hayward fault is continuous at depth, extending southward below the Evergreen fault and connecting the Hayward fault to the Calaveras fault, then this extension could possibly contribute additional moment release to a rupture of the southern Hayward fault. Andrews *et al.* (1993) recognized that the dip-slip moment released is not sufficient to account for all the accumulated contractional strain, and therefore there is an additional threat from reverse faulting in the region. They calculated a M_W 6.3 earthquake on the Mission fault due to dip slip alone. If contractional strain is accumulating even further southward on the Hayward-Evergreen frontal reverse system, an even larger earthquake is possible if the entire length of the fault and its accumulated moment is released in a single event. Additionally, the rupture of the southern Hayward-Evergreen fault in a strike-slip mode would release more moment than just the southern Hayward fault alone. The Working Group on California Earthquake Probabilities (2003) estimate a mean M_W 6.7 earthquake on the southern Hayward fault (with a M_W 6.9 event at the upper bound of the 95% confidence interval), including the probability that rupture extends along the Evergreen fault to Alum Rock.

Our model suggests that the Mission and Alum Rock seismic trends represent a continuous transition from the near-vertical Hayward fault to a dipping Hayward-

Evergreen fault system that splays off the Calaveras fault. Although rupture propagating from the Calaveras fault to the Hayward fault through the restraining bend is unlikely, an event originating on the Calaveras fault may hasten rupture on the Evergreen and subsequently the southern Hayward fault. Therefore, the interaction between Calaveras and Hayward faults needs to be considered for seismic hazard assessments.

Conclusions

Our 3D V_p model, hypocentral relocations, and recomputed focal mechanisms, combined with gravity and aeromagnetic data and geologic data, suggest a structural and kinematic model that explains the uplift of the Mission Hills and the transfer of slip between the Calaveras and Hayward faults. Our interpretation accommodates the transfer of slip through a Hayward fault that splays off the Calaveras fault near the location where the Alum Rock seismic trend diverges from the Calaveras fault seismicity. The Hayward fault, projecting further south to include the Evergreen fault system acts as a bounding surface between the San Francisco Bay block and the Mission Hills. As the San Francisco Bay block translates northward, it is wedging under the Mission Hills and producing the region of contraction. This model lends support to the seismic source characterization and models previously proposed by the Working Group on Northern California Earthquake Potential (1996) and the Working Group on California Earthquake Probabilities (1999, 2003). However, it suggests that the Calaveras and Hayward faults are part of a single system and this relationship needs to be considered for seismic hazard assessment.

Acknowledgments

We thank David Oppenheimer, Tom Parsons, Tom Brocher, Robert Simpson, Dave Ponce, Robert Jachens, Russ Graymer, and Joe Andrews at the U.S. Geological Survey for their reviews and comments throughout this project. We also thank Tom Brocher for providing BASIX shot data for this experiment. We acknowledge Donna Eberhart-Phillips for her help with the SIMULPS12 code and visualization of the resolution spread. We also acknowledge Donna Eberhart-Phillips, Cliff Thurber, and John Evans for their contributions in creating and maintaining the SIMULPS12 code. Finally, we thank David Oppenheimer and Keith Kelson for reviewing this manuscript and their suggestions to make it better.

We also recognize the Northern California Earthquake Data Center for providing public access to seismologic data, and their contributors at the Berkeley Seismological Laboratory of the University of California and the Northern California Seismic Network maintained by the U.S. Geological Survey, Menlo Park. Finally, we thank Robert Jachens and Russ Graymer of the U.S. Geological Survey for providing input on the gravity, aeromagnetic, and geological data in the region. This work was funded in part by a grant from the U.S. Geological Survey National Earthquake Hazards Reduction Program (Grant 99HQGR0066).

References

Andrews, D. J., D. H. Oppenheimer, and J. J. Lienkaemper (1993). The Mission link between the Hayward and Calaveras faults, *J. Geophys. Res.* **98,** no. B7, 12,083–12,095.

Aydin, A., and B. Page (1984). Diverse Pliocene-Quaternary tectonics in a transform environment, San Francisco Bay Region, California, *Geol. Soc. Am. Bull.* **95,** 1303–1317.

Blumling, P., W. D. Mooney, and W. H. K. Lee (1985). Crustal structure of the southern Calaveras fault zone, central California, from seismic refraction investigations, *Bull. Seism. Soc. Am.* **75,** 193–209.

Brocher, T. M., M. J. Moses, and S. D. Lewis (1992). Wide-angle seismic recordings obtained during seismic reflection profiling by the S. P. Lee offshore the Loma Prieta epicenter, *U.S. Geol. Surv. Open-File Rept. 92-245*.

Bürgmann, R., D. Schmidt, R. M. Nadeau, M. d'Alessio, E. Fielding, D. Manaker, T. V. McEvilly, and M. H. Murray (2000). Earthquake potential along the Northern Hayward fault, California, *Science* **289,** no. 5482, 1178–1182.

California Division of Mines and Geology (1996). Probabilistic seismic hazard assessment for the State of California, *Calif. Dept. Conserv. Div. Mines Geol.* and *U.S. Geol. Surv., CDMG Open-File Rept. 96-08* (*USGS OFR 96-706*).

Christie-Blick, N., and K. T. Biddle (1985). Deformation and basin formation along strike-slip faults, in Strike-Slip Deformation, Basin Formation, and Sedimentation, N. Christie-Blick and K. T. Biddle, editors, *Soc. Econ. Paleon. Miner. Spec. Pub.* **37,** 1–37.

Dibblee, T. W., Jr. (1980). Preliminary geologic map of the Niles quadrangle, Alameda County, California, *U.S. Geol. Surv. Open-File Rept. 80-533c*, scale 1:24,000.

Dorbath, C., D. Oppenheimer, F. Amelung, and G. King (1996). Seismic tomography and deformation of the junction of the San Andreas and Calaveras faults, *J. Geophys. Res.* **101,** no. B12, 27,917–27,941.

Eberhart-Phillips, D., and A. J. Michael (1998). Seismotectonics of the Loma Prieta region determined from three-dimensional V_p, V_p/V_s, and seismicity, *J. Geophys. Res.* **103,** no. B9, 21,099–21,120.

Ellsworth, W. L. (1990). Earthquake history, 1769–1989, in *The San Andreas Fault System, California*, R. E. Wallace (Editor), *U.S. Geol. Surv. Profess. Pap. 1515*, 153–188.

Ellsworth, W. L., J. A. Olson, L. N. Shinjo, and S. M. Marks (1982). Seismicity and active faults in the eastern San Francisco Bay region, in *Proceedings of the Conference on Earthquake Hazards in the Eastern San Francisco Bay Region, Spec. Pub. Calif. Div. Mines Geol.* **62,** 83–91.

Evans, J. R., D. Eberhart-Phillips, and C. H. Thurber (1994). User's manual for SIMULPS12 for imaging v_p and v_p/v_s. A derivative of the "Thurber" tomographic inversion SIMUL3 for local earthquakes and explosions, *U.S. Geol. Surv. Open-File Rept. 94-431*, 101 pp.

Graymer, R. W., D. L. Jones, and E. E. Brabb (1995). Geology of the Hayward fault zone: A digital map database, *U.S. Geol. Surv. Open-File Rept. 95-597*, 16 pp.

Graymer, R. W., D. L. Jones, and E. E. Brabb (1996). Preliminary geologic map emphasizing bedrock formations in Alameda County, California: A digital database. *U.S. Geol. Surv. Open-File Rept. 96-252*, 14 pp.

Graymer, R. W., D. L. Jones, E. E. Brabb, and E. J. Helley (1994). Preliminary geologic map of the Niles 7.5-minute quadrangle, Alameda County, California, *U.S. Geol. Surv. Open-File Rept. 94-132*.

Hall, C. A. (1958). Geology and paleontology of the Pleasanton area, Alameda and Contra Costa counties, University of California Press, 1 map, scale 1:40,000, 63 pp.

Harbert, W., and A. Cox (1989). Late Neogene motions of the Pacific plate, *J. Geophys. Res.* **94,** no. B3, 3056–3064.

Hardebeck, J. L., J. Boatwright, D. Dreger, R. Goel, V. Graizer, K. Hudnut, C. Ji, L. Jones, J. Langbein, J. Lin, E. Roeloffs, R. Simpson, K. Stark, R. Stein, and J. C. Tinsley (2004). Preliminary report on the 22 December 2003, M6.5 San Simeon, California earthquake, *Seism. Res. Lett.* **75,** no. 2, 155–172.

Hauksson, E., L. M. Jones, T. L. Davis, K. Hutton, A. G. Brady, P. A. Reasenberg, A. J. Michael, and R. F. Yerkes (1988). The 1987 Whittier Narrows earthquake in the Los Angeles metropolitan area, California, *Science* **239,** no. 4846, 1409–1412.

Hauksson, E., L. M. Jones, and K. Hutton (1995). The 1994 Northridge

earthquake sequence in California: Seismological and tectonic aspects, *J. Geophys. Res.* **100,** no. B7, 12,335–12,355.

Hill, D. P., J. P. Eaton, and L. M. Jones (1990). Seismicity, 1980–1986, in *The San Andreas Fault System, California*, R. E. Wallace (Editor) *U.S. Geol. Surv. Profess. Pap. 1515*, 115–151.

Holbrook, W. S., T. M. Brocher, U. S. ten Brink, and J. A. Hole (1996). Crustal structure of a transform plate boundary: San Francisco Bay and the central California continental margin, *J. Geophys. Res.* **101,** no. B10, 22,311–22,334.

Jachens, R. C., and C. W. Roberts (1993). Aeromagnetic map of the San Francisco Bay area, California, *U.S. Geol. Surv. Geophys. Investigations Map GP-1007*, 1 sheet, scale approximately 1:286,500.

Jennings, C. W. (1994). Fault activity map of California and adjacent areas, Calif. Div. Mines Geol., Geologic data map No. 6, 1 sheet, scale 1:750,000, with explanatory text (92 pp.), 1 plate.

Jones, D. L., R. Graymer, C. Wang, T. V. McEvilly, and A. Lomax (1994). Neogene transpressive evolution of the California Coast Ranges, *Tectonics* **13,** no. 2, 561–574.

Kafka, A. L., and S. Z. Levin (2000). Does the spatial distribution of smaller earthquakes delineate areas where larger earthquakes are likely to occur? *Bull. Seism. Soc. Am.* **90,** no. 3, 724–738.

Kelson, K. I., G. D. Simpson, C. C. Haraden, T. L. Sawyer, and M. A. Hemphill-Haley (1993). Late Quaternary surficial deformation of the southern East Bay Hills, in *Final Technical Report: National Earthquake Hazards Reduction Program*, *U.S. Geol. Surv.*, William Lettis & Associates, Inc. and Woodward-Clyde Federal Services, 29 pp.

Kelson, K. I., G. D. Simpson, W. R. Lettis, and C. C. Haraden (1996). Holocene slip rate and earthquake recurrence of the northern Calaveras fault at Leyden Creek, California, *J. Geophys. Res.* **101,** no. B3, 5691–5975.

Kissling, E. (1995). Program VELEST user's guide: Institute of Geophysics, ETH Zurich. 25 p., Appendix. For the Fortran77 program VELEST v. 3.1, Inst. of Geophys. Swiss Seis. Service, ETH-Hoenggeberg, Zurich, Switzerland.

Koltermann, C. E., and S. M. Gorelick (1992). Paleoclimate signature in terrestrial flood deposits, *Science* **256,** no. 5065, 1775–1782.

Kostrov, B. V. (1974). Seismic moment and energy of earthquakes, and seismic flow of rock, *Izv. Acad. Sci. USSR Phys. Solid Earth 1* 23–24.

Kraus, M. (2003). LiveGraphics3D, internet download at www.vis.uni-stuttgart.de/~kraus/LiveGraphics3D/download.html (last accessed December 2003).

Lienkaemper, J. J. (1992). Map of recently active traces of the Hayward fault, Alameda and Contra Costa counties, California. U.S. Geol. Surv. Misc. Field Study Map MF-2196, scale 1:24,000, 1 plate, 13 pp.

Lienkaemper, J. J., and J. S. Galehouse (1997). Revised long-term creep rates on the Hayward fault, Alameda and Contra Costa counties, California, *U.S. Geol. Surv. Open-File Rept. 97-690*, 18 pp.

Lienkaemper, J. J., G. Borchardt, and M. Lisowski (1991). Historic creep rate and potential for seismic slip along the Hayward fault, California, *J. Geophys. Res.* **96,** no. B11, 18,261–18,283.

McClay, K., and M. Bonora (2001). Analog models of restraining stepovers in strike-slip fault systems, *Bull. Am. Assoc. Petrol. Geol.* **85,** no. 2, 233–260.

Menke, W. (1989). *Geophysical data analysis: Discrete inverse theory*, Revised Edition, Vol. **45,** 289 pp., in International Geophysics Series, Academic Press, New York.

Michael, A. J. (1988). Effects of three-dimensional velocity structure on the seismicity of the 1984 Morgan Hill, California, aftershock sequence, *Bull. Seism. Soc. Am.* **78,** no. 3, 1199–1221.

Michael, A. J., and D. Eberhart-Phillips (1991). Relations among fault behavior, subsurface geology, and three-dimensional velocity models, *Science* **253,** 651–654.

Michelini, A., and T. V. McEvilly (1991). Seismological studies at Parkfield, part I: Simultaneous inversion for velocity structure and hypocenter using cubic b-splines parameterization, *Bull. Seism. Soc. Am.* **81,** 524–552.

Oppenheimer, D. H., W. H. Bakun, and A. G. Lindh (1990). Slip partitioning of the Calaveras fault, California, and prospects for future earthquakes, *J. Geophys. Res.* **95,** no. B6, 8483–8498.

Oppenheimer, D. H., R. A. Reasenberg, and R. W. Simpson (1988). Fault plane solutions for the 1984 Morgan Hill, California, earthquake sequence: evidence for the state of stress on the Calaveras fault, *J. Geophys. Res.* **93,** no. B8, 9007–9026.

Page, B. M., G. A. Thompson, and R. G. Coleman (1998). Late Cenozoic tectonics of the central and southern Coast Ranges, *Bull. Geol. Soc. Am.* **110,** no. 7, 846–876.

Parsons, T., and P. E. Hart (1999). Seismic-reflection evidence that the Hayward fault extends into the lower crust of the San Francisco Bay area, California, *Geology* **27,** no. 9, 839–842.

Ponce, D. A., T. G. Hildenbrand, and R. C. Jachens (2003), Gravity and magnetic expression of the San Leandro gabroo with implications for the geometry and evolution of the Hayward fault zone, northern California, *Bull. Seism. Soc. Am.* **93,** no. 1, 14–26.

Reasenberg, P, and D. Oppenheimer (1985). FPFIT, FPPLOT and FPPAGE: Fortran computer programs for calculating and displaying earthquake fault-plane solutions, *U.S. Geol. Surv. Open-File Rept. 85-739.*

Roberts, C. W., and R. C. Jachens (1993). Isostatic residual gravity map of the San Francisco Bay area, California, *U.S. Geol. Surv. Geophys. Investigations Map GP-1006*, 1 sheet, scale approximately 1:286,500.

Rubin, A. (2002). Aftershocks of microearthquakes as probes of the mechanics of rupture, *J. Geophys. Res.* **107,** no. B7, doi 10.1029/2001JB000496.

Schaff, D. P., G. H. R. Bokelmann, G. C. Beroza, F. Waldhauser, and W. L. Ellsworth (2002). High resolution image of Calaveras fault seismicity, *J. Geophys. Res.* **107,** no. B9, doi 0.1029/2001JB000633.

Simpson, R. W., J. J. Lienkaemper, and J. S. Galehouse (2001). Variations in creep rate along the Hayward fault, California, interpreted as changes in depth of creep, *Geophys. Res. Lett.* **23,** no. 11, 2269–2272.

Sipkin, S. A., and R. E. Needham (1990). Kinematic source parameters determined by time-dependent moment-tensor inversion and an analysis of teleseismic first motions, in *The Coalinga, California, Earthquake of May 2, 1983*, M. J. Rymer and W. L. Ellsworth (Editors), *U.S. Geol. Surv. Profess. Pap. 1487*, 207–213.

Thurber, C. H. (1983). Earthquake locations and three-dimensional crustal structure in the Coyote Lake area, central California, *J. Geophys. Res.* **88,** no. B10, 8226–8236.

Twiss, R. J., and E. M. Moores (1992). *Structural Geology*, Freeman, W. H., New York, 532 pp.

Wagner, D. L., E. J. Bortugno, and R. D. McJunkin (1990). Geologic map of the San Francisco-San Jose quadrangle, Calif. Dept. of Conserv., Div. Mines Geol., Reg. Geol. Map Ser, Map no. 5A, scale 1:250,000, 5 sheets.

Westaway, R. (1995), Deformation around stopovers in strike-slip fault zones, *J. Struct. Geol.* **17,** no. 6, 831–846.

Wong, I. G., and M. A. Hemphill-Haley (1992). Seismicity and faulting near the Hayward and Mission faults, in *Proceedings of the Second Conference on Earthquake Hazards in the Eastern San Francisco Bay Area*, Calif. Dept. Conserv., Div. Mines Geol., Special Pub. 113, 207–215.

Woodcock, N. H., and M. Fischer (1986). Strike-slip duplexes, *J. Struct. Geol.* **8,** no. 7, 725–735.

Working Group on California Earthquake Probabilities (1999). Earthquake probabilities in the San Francisco Bay region: 2000 to 2030—a summary of findings, *U.S. Geol. Surv. Open-File Rept. 99-517*, 36 pp.

Working Group on California Earthquake Probabilities (2003). Earthquake probabilities in the San Francisco Bay region: 2002 to 2031, *U.S. Geol. Surv. Open-File Rept. 03-214*, 235 pp.

Working Group on Northern California Earthquake Probabilities (1996). Database of potential sources for earthquakes larger than magnitude 6 in northern California, *U.S. Geol. Surv. Open-File Rept. 96-705*, 29 pp.

Zhang, H., and C. H. Thurber (2003). Double-difference tomography: the method and its application to the Hayward fault, California, *Bull. Seism. Soc. Am.* **93,** no. 5, 1875–1889.

Department of Geology
University of California, Davis
1 Shields Avenue
Davis, California 95616
manaker@geology.ucdavis.edu
(D.M.M.)

Western Earthquake Hazards Team
U.S. Geological Survey
345 Middlefield Road, M/S 977
Menlo Park, California 94025-3591
michael@usgs.gov
(A.J.M.)

Department of Earth and Planetary Science
University of California, Berkeley
385 McCone Hall
Berkeley, California 94720
burgmann@seismo.berkeley.edu
(R.B.)

Manuscript received 1 October 2002.